The Thesis committee for Amir Toliyat

Certifies that this is the approved version of the following thesis:

Modeling and Simulation of Distribution System Components in Anticipation of a Smarter Electric Power Grid

APPROVED BY
SUPERVISING COMMITTEE:

Supervisor: Alexis Kwasinski

W. Mack Grady

Modeling and Simulation of Distribution System Components in Anticipation of a Smarter Electric Power Grid

by

Amir Toliyat, B.S.

Thesis

Presented to the Faculty of the Graduate School of

The University of Texas at Austin

in Partial Fulfillment

of the Requirements

for the Degree of

Master of Science in Engineering

The University of Texas at Austin

May 2011

To my family: my parents *Hamid* & *Mina* and my brother *Mohammad*

Acknowledgments

The author would like to thank Dr. Alexis Kwasinski for his patience and continued support throughout the completion of this thesis. Dr. Kwasinski's valuable guidance, relentless work ethic, and consummate professionalism have provided great inspiration in achieving academic success.

The author would also like to thank his colleagues in the Power Electronics Research Group, namely Chimaobi Onwuchekwa, Vaidyanathan Krishnamurthy, Juyoung Jung, Sungwoo Bae, Seung Choung, Ted Song, Ruichen Zhao, Seunghyun Chun, Sheng-Yang Yu, and Harsha Kumar for various help throughout this research.

May 6th, 2011

Modeling and Simulation of Distribution System Components in Anticipation of a Smarter Electric Power Grid

by

Amir Toliyat, M.S.E.

The University of Texas at Austin, 2011

Supervisor: Alexis Kwasinski

Successful development of the electric power grid of the future, hereinafter referred to as a smart grid, implicitly demands the capability to model the behavior, performance, and cost of distribution-level smart grid components. The modeling and simulation of such individual components, together with their overall interaction, will provide a foundation for the design and configuration of a smart grid.

It is the primary intent of this thesis, to provide a basic insight into the energy transfer of various distribution-level components by modeling and simulating their dynamic behavior. The principal operations of a smart grid must be considered, including variable renewable generation, energy storage, power electronic interfaces, variable load, and plug-in electric vehicles. The methodology involves deriving the mathematical equations of components, and, using the MATLAB/Simulink environment, creating modules for each component. Ultimately, these individual modules may be connected together via a voltage interface to perform various analyses, such as the treatment of harmonics, or to acquire an understanding of design parameters such as capacity, runtime, and optimal asset utilization.

Table of Contents

List of Tables

List of Figures

Chapter 1: Introduction

As the demand for electricity continuously grows, its generation, transmission, and distribution must provide accordingly in order to sustain the economy and way of life. This means that the grid, already aging and becoming frailer, will experience even more stress. Although the rapid growth in technology throughout past decades has been humbling—from advances in wireless communication and television, to impressive improvements in automobiles and aviation—one major network, the grid, has remained stagnant in its development. In fact, much of the current grid was designed over 60 years ago, making it outdated in comparison.

1.1 THE CURRENT GRID

As an expansive network responsible for many critical infrastructures, including energy, communications, transportation, water, and food supply, it is no surprise why the grid, as it exists today, is so vital yet so vulnerable. Many of the components of the grid are susceptible to both natural and man-made disasters. The transmission system alone is a reason for concern, as more than 150,000 miles of it extend unprotected across bare countryside [1]. Today's grid supports the generation, transmission, distribution, and control of electricity; however, there are several means of accomplishing these, as will be discussed later. Electricity is generated from various forms of energy, be it coal, natural gas, or nuclear, to name a few. After its generation, the electricity is stepped up to a higher voltage, where it is subsequently transmitted over relatively long distances. Once transmitted, it arrives at a substation, where it is stepped down in voltage, then distributed within the distribution network; some of the common "standard" distribution voltage levels are 34.5 kV, 23.9 kV, 14.4 kV, 13.2 kV, 12.47 kV, and 4.16 kV [2]. Finally, the electricity is stepped down once again from the distribution-level voltage to the necessary service voltage.

The existing structure of most distribution networks is radial, as depicted in Fig. 1. In this topology, power is transferred in only one direction from a particular source to various delivery points. Although this is the cheapest and simplest topology, its disadvantage is that a disruption

or failure at any location in the network affects all downstream customers. Another characteristic of the existing grid is that the generation and consumption of electricity must be balanced, because electricity is consumed nearly instantly after it is generated. The drawback of this is that, in the event of a large uncompensated failure in the grid, the power delivered from generators are rerouted over transmission lines that do not have the capacity to maintain the excess electricity, resulting in further failures. An additional disadvantage of the generation-consumption interdependency is that any surplus energy would be wasted if it were not consumed almost immediately.

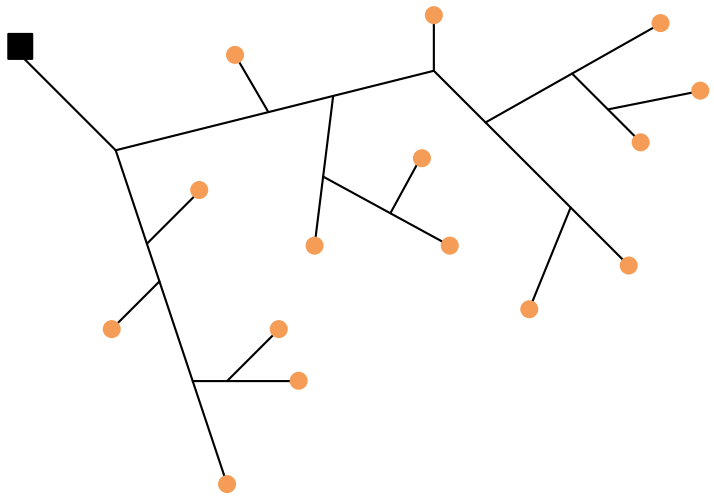

Figure 1: Radial distribution grid topology (black square represents point of generation; orange dots represent points of consumption)

An alternative to the radial topology is the mesh network topology shown in Fig. 2. Here, power flow is not constrained to only one direction. Also, not only is each node responsible for consuming its own power, but it must also collaborate with other nodes to propagate power in the network. Therefore, in the event of a failure to a portion of the grid, the nodes can reroute power to the affected area, so that customers are not left without power for long periods of time.

Although more reliable in contrast to the radial topology, the mesh network is more expensive and more complex.

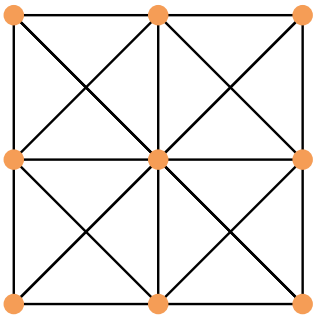

Figure 2: Mesh network distribution grid topology (orange dots represent points of consumption)

The introduction of new technologies such as renewable energy sources, plug-in electric vehicles, and energy storage is reshaping the traditional model of a distribution network, as well as how, when, and where power is delivered. A modernized grid is not only desirable, but also necessary, because the current grid is becoming increasingly unreliable. Within the past 40 years, five massive blackouts have resulted from grid failure—three of which have been in the past decade alone [3]. The economic cost associated with such events is tremendous, which is only one of the many reasons why the grid must be revamped.

1.2 TOWARD A MODERN GRID

Taking into account that the present means of producing and consuming energy may not suffice for long, it is advised that certain improvements be made in order to fulfill society's growing demand for electricity, and in so doing, develop a more stable grid. Several goals have been instituted for an advanced grid of the 21st century. In particular, a modern grid will be safer, more reliable, more secure, more economic, more efficient, and more environmentally friendly [4]. By equipping distribution systems with digital technology, allowing for a real-time two-way flow of energy and data, integrating renewable energy sources and energy storage, increasing

distributed generation, and heightening user-controlled power management, the concept of a smart, modern grid can become reality.

A desirable feature of a smart grid is the ability of consumers to return excess power to the grid. For this to be accomplished, renewable energy sources such as solar and wind power must be integrated into the distribution system, where home or business owners seek to actively manage consumption based on real-time information regarding energy usage. However, an important consideration is that solar and wind are variable power sources, which may be available when not needed, or conversely, may not be available when needed. To overcome this variability in supply, energy storage technologies should be employed to make the system more predictable and to enable more efficient use of resources. Furthermore, energy storage is also conducive to maintaining the balance between generation and consumption. As mentioned previously, the balance between generation and consumption must be sustained if the power system is to remain stable. If this balance is disturbed, the dynamics of generators and loads can cause the system frequency and/or voltages to vary, leading to system collapse [5]. Thus, energy storage provides an additional degree of flexibility welcomed in a system where variability is not only evident in the load profile, but also in the supply side. Additionally, as the adoption of plug-in electric vehicles becomes more widespread, their batteries will likely be considered as distributed mobile storage, rendering them an important feature of a modernized distribution grid. These vehicles also provide a benefit of reducing the burden placed on the grid, as consumers will be encouraged to charge their vehicles at night, i.e., off-peak, and later dispatch the power back into the grid during the day when the vehicles are parked at home or at work. The integration of these technologies will undoubtedly alter the conventional design of the grid and may lead to an architecture resembling that shown in Fig. 3.

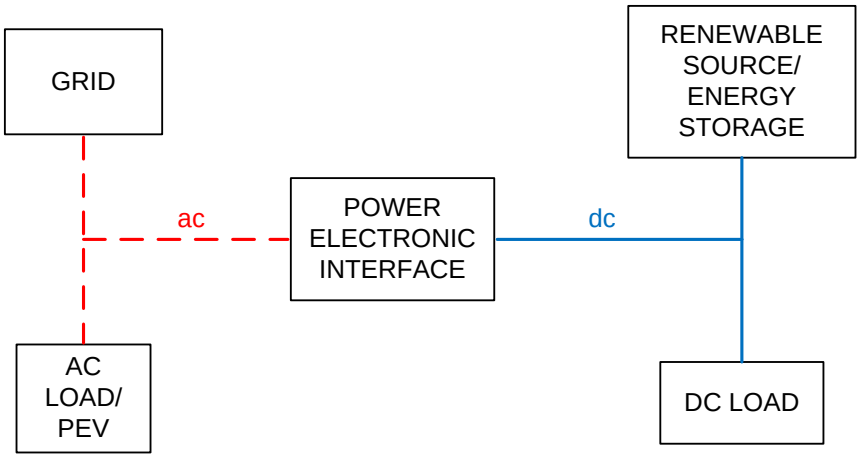

Figure 3: Potential smart grid architecture

A smart grid provides opportunities to be more efficient and more economic by minimizing grid operator response time. One manner in which a smart grid promotes efficiency is through its network of smart meters and controls that are widely installed within the grid. This allows for the constant relay of information and hence enables operators to be aware of the grid's behavior at any one time. Such a scenario is much more favorable than the current situation, where delays often result from consumers having to call operators to inform them of a power outage. The inefficiency inherent in these delays represents wasted time and valuable productivity. The smart meters and controls, together with the mesh network topology described earlier, can empower the grid to make automated, self-healing decisions. Additionally, the opportunity to be more efficient emerges from how electricity is presently delivered. That is, by knowing exactly how much energy is needed minute by minute, operators can avoid flooding the lines with electricity. Flooding the lines with electricity is undesirable because the information-deprived electricity delivered by the operator is often more than needed; therefore, its allocation is deemed inefficient.

Moreover, a modernized grid will also ensure greater security, as it will facilitate a less centralized infrastructure that is less prone to threats and attack. When considering the

potentially catastrophic effects a seemingly harmless tree branch can have on a large portion of the network, the vulnerabilities of the grid become glaringly evident. Even more worrisome is the prospect of much more malicious intentions such as cyber-attacks or terrorism. In the event of such perils, ordinary living conditions are considerably affected—delivery systems for oil and water cannot function, communication capabilities may be unavailable, rail and air travel is disrupted, and homeland security is jeopardized. At the home and business level, the lack of air conditioning creates unfavorable circumstances for survival. However, with the benefits of a smart grid, electricity can be supplied from hundreds of distributed sources, and, via advanced controls and communication, rerouted and restored quickly, thus providing for critical loads and avoiding large-scale outages.

The advantages of a clean-energy smart grid are undeniably vast; they encompass the expansion of renewable electricity, increased reliability and security, and enhanced energy efficiency. However, without properly understanding and modeling the impact of smart grids, these ambitious priorities cannot be advanced.

1.3 PURPOSE AND ORGANIZATION OF THESIS

This thesis develops a framework for modeling a modernized distribution grid. The MATLAB/Simulink software package is used to model and analyze the dynamic response of various distribution-level components intended to constitute a smart grid. The approach taken involves creating what will be referred to as ‘blocks’ for the individual components, where each block masks the mathematical, or, where applicable, dynamic equations of the associated component. The motivation behind such an approach is to produce an environment whereby the components can eventually interface together to represent certain portions of an advanced distribution grid. The specific components concerned with in this thesis include photovoltaic arrays, the electric grid, a load representative of a typical air-conditioning unit, conductor cables (ac and dc), batteries for energy storage (charging and discharging modes), plug-in electric vehicles, and power electronic interfaces (buck converter, boost converter, rectifier, inverter).

Chapter 2 and Chapter 3 are parallels of one another, in that the modeling of components is explained in the former, and the simulations/results of the proposed models are evaluated in the latter.

Chapter 4 concludes the thesis and mentions improvements and suggestions for future work.

Chapter 2: Modeling of Components

This chapter details the modeling of various distribution system components by deriving their dynamic equations (where applicable). The mathematical equations derived in this chapter will be used in the subsequent chapter to create modules, or 'blocks', that represent each component. Parameters of interest for the components include voltage, current, and power (generated/consumed/transferred).

2.1 PHOTOVOLTAIC ARRAY

Photovoltaic (PV) power generation is a viable solution for promoting distributed generation, reducing carbon emissions, and satisfying the overall obligation for a modernized grid. It is therefore essential that the grid be expanded to support significant increases in the penetration of renewable energy. Dynamic modeling and simulation of PV arrays are important for predicting energy production and making informed technical and economic decisions. Furthermore, since PV systems are usually deployed in a highly dispersed fashion and in the lowest voltage portions of the grid, they represent challenges for understanding how their high penetration levels might impact system operations [6].

The model developed in this thesis is an adaptation from [7], with several modifications that contribute to the pertinence of the analysis intended for in this work. As with any PV array, the equation describing the *I-V* characteristic of an ideal PV cell is

$$I = I_{pv,cell} - \underbrace{I_{0,cell}\left[\exp\left(\frac{qV}{akT}\right) - 1\right]}_{I_d} \tag{2.1}$$

where $I_{pv,cell}$ is the current generated by the incident light, I_d is the Shockley diode equation, $I_{0,cell}$ is the reverse saturation current of the diode, q is the electron charge, k is the Boltzmann constant, T (in Kelvin) is the temperature of the *p-n* junction, and a is the diode ideality constant

[7]. In reality, however, (2.1) does not accurately represent practical PV arrays; therefore, the inclusion of additional parameters is required according to the following equation [8]:

$$I = I_{pv} - I_0\left[\exp\left(\frac{V + R_s I}{V_t a}\right) - 1\right] - \frac{V + R_s I}{R_p} \tag{2.2}$$

where I_{pv} and I_0 are the photovoltaic and saturation currents, respectively, of the array, $V_t = N_s kT/q$ is the thermal voltage of the array with N_s cells connected in series, R_s is the equivalent series resistance of the array, and R_p is the equivalent parallel resistance of the array [7]. The relationship between an ideal PV device and a practical one is illustrated in Fig. 4.

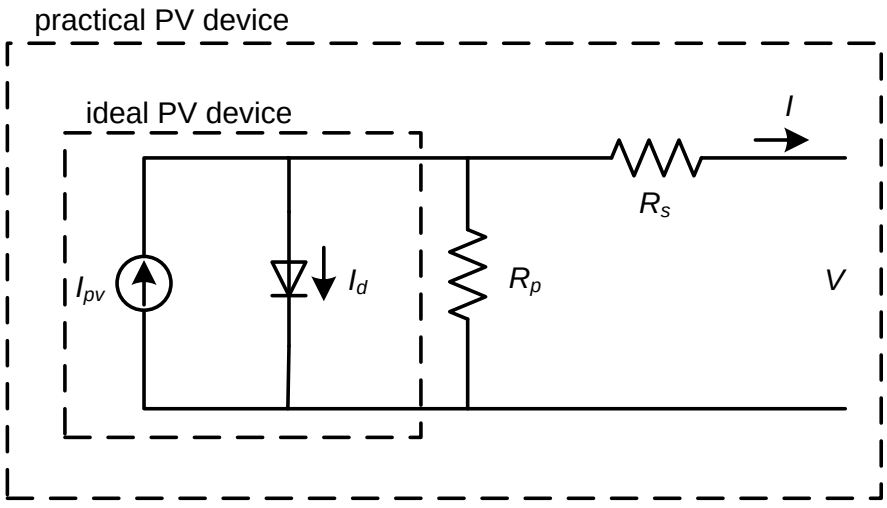

Figure 4: Relationship between an ideal PV device and a practical PV device

Although more sophisticated models in [9]-[14], as well as more simplified models in [15]-[21] have been proposed, the single-diode model of the practical PV device shown in Fig. 4 offers a good compromise between simplicity and accuracy, and has frequently been used by authors in other works [22]-[36]. The more sophisticated models involve two-diode or three-diode topologies, whereas the more simplified models neglect resistances R_p and R_s. The light-

generated current of the PV cell, I_{pv}, in (2.2) depends on the temperature and solar irradiation, and is derived according to [32], [37]-[39]

$$I_{pv} = \left(I_{pv,n} + K_I \Delta_T\right)\frac{G}{G_n} \tag{2.3}$$

where $I_{pv,n}$ is the light-generated current at the nominal condition (usually 25^{o}C and 1000 W/m^2), K_I is the short-circuit current/temperature coefficient, $\Delta_T = T\text{-}T_n$ (T and T_n being the actual and nominal temperatures [in Kelvin], respectively), G (watts per square meters) is the irradiation on the device surface, and G_n is the nominal irradiation [7]. Lastly, the diode saturation current, I_0, in (2.2) may be expressed by [37], [38], [40]-[43]

$$I_0 = \frac{I_{sc,n} + K_I \Delta_T}{\exp\left[\left(V_{oc,n} + K_V \Delta_T\right)/ aV_t\right] - 1} \tag{2.4}$$

where $I_{sc,n}$ is the nominal short-circuit current, $V_{oc,n}$ is the nominal open-circuit voltage, and K_V is the open-circuit voltage/temperature coefficient [7].

PV array datasheets typically provide values for $V_{oc,n}$, $I_{sc,n}$, V_{mp}, I_{mp}, K_V, and K_I. However, the parameters R_s and R_p in (2.2) remain unknown, and their solution, which is not within the scope of this thesis, is obtained iteratively as in [7]. After deriving R_s and R_p, the light-generated current at nominal condition can be solved for according to:

$$I_{pv,n} = \frac{R_p + R_s}{R_p} I_{sc,n} \tag{2.5}$$

At this point all parameters are known, and the model current I_m, which represents the difference between I_{pv} and I_d in Fig. 4, is obtained and shown in Fig. 5. Additionally, the array is assumed to be operating at the maximum power point; therefore, using the values available from the datasheet, the load resistance can be expressed as:

$$R_{load} = \frac{N_{ss}}{N_{pp}} \cdot \frac{V_{mp}}{I_{mp}} \tag{2.6}$$

where N_{ss} and N_{pp} are the number of series and parallel modules, respectively, in the array. As opposed to [7], where the model generates the *I-V* curve of the array, the results of interest in this thesis include the operating voltage and operating current, as well as the total power generated by the PV array. These parameters are obtained by combining (2.6) with the circuit model in Fig. 5, resulting in the equations of the PV array:

$$\begin{cases} x_1 = \dfrac{x_2}{R_{load}} = \dfrac{x_2}{\left(\dfrac{N_{ss}}{N_{pp}} \cdot \dfrac{V_{mp}}{I_{mp}}\right)} \\ x_2 = \left[\left(\left(I_m - x_1\right) \cdot R_p \cdot \dfrac{N_{ss}}{N_{pp}}\right) - \left(x_1 \cdot R_s \cdot \dfrac{N_{ss}}{N_{pp}}\right)\right] \\ P = x_1 \cdot x_2 \end{cases} \tag{2.7}$$

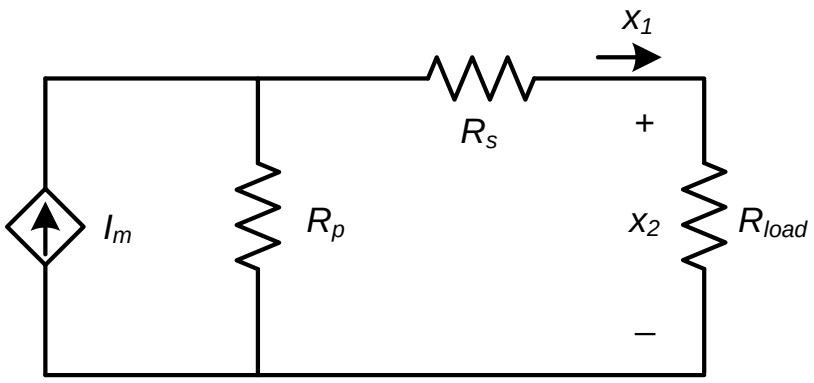

Figure 5: Equivalent-circuit model of Fig. 4. (I_m is a function of solar irradiance and temperature)

2.2 ELECTRIC GRID

Modeling the grid is necessary for analyzing its interaction with other components. The grid is the main infrastructure for delivering electricity, and this burden can be reduced with widespread integration of renewable energy, energy storage, and advanced communication and monitoring technologies. Therefore, modeling the grid is important because it provides insight into the amount of electricity required, given supply and demand.

The grid, whose circuit model is depicted in Fig. 6, can be represented by a Thevenin equivalent circuit consisting of an ideal voltage source V_{ac} and equivalent impedance Z_{eq}. The equivalent impedance is often referred to as the short-circuit impedance since it is calculated from the short-circuit capacity at the bus where the equivalent circuit is to be placed [44]. The short-circuit impedance is indicated by an inductor in Fig. 6, because the power system source is more inductive than capacitive. Hence, this impedance may often be called the short-circuit reactance as well. R_{load} and L_{load} represent the resistive and inductive components of the collective equivalent load connected to the grid.

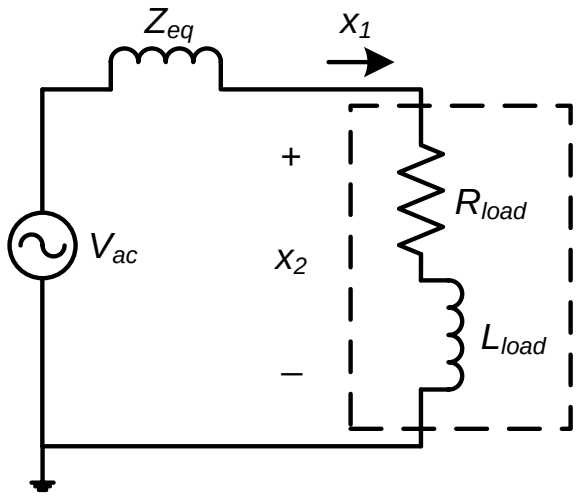

Figure 6: Circuit model of electric grid

Taking x_1 to be the current drawn from the grid and x_2 to be the grid voltage, the dynamic equations are derived as follows:

$$\begin{cases} \dot{x}_1 = \dfrac{V_{ac} - R_{load} \cdot x_1}{Z_{eq} + L_{load}} \\ x_2 = V_{ac} - Z_{eq} \cdot \dot{x}_1 \end{cases} \tag{2.8}$$

In order to obtain the power consumed from the grid, the power factor must first be calculated according to:

$$p.f. = \cos\left[\tan^{-1}\left(\frac{2\pi \cdot f \cdot L_{load}}{R_{load}} \right) \right] \tag{2.9}$$

Thus, it follows that:

$$P = x_1 \cdot x_2 \cdot p.f. \tag{2.10}$$

It should be noted that the above is only true for circuits with single frequency waveforms, and may not be true when harmonic-producing power electronics circuits are added. Since the grid is modeled as a linear component in this thesis, (2.10) is valid.

2.3 LOAD

One important issue to assess in modeling a distribution system is the demand for electricity, or load, which is the driving force on the power system. The load on a power system results in response to the processes taking place in devices or appliances. Since not enough is known about the load characteristics and their fairly random nature, simplifying assumptions have been made so far to model loads in various power system studies [45].

Air conditioning comprises a major portion of the total residential load, especially during the summer. Therefore, controlling air conditioning offers potentials for controlling the total load on the system. This is where load management promises to have positive outcomes in a smart grid, where customer electric loads are controlled during times of peak usage. By controlling equipment such as air conditioning, load management helps in shifting the load peak to times when customers do not use as much electricity. Load management strategies, which are cost driven and rely on timely information, reduce the peaks and valleys in the demand profile, hence making it ideally constant [46]. Aside from the detrimental impacts related to cost, efficiency, and resources, an overwhelming air conditioning load may lead to voltage instability, and ultimately, system collapse [47]-[49]. In this thesis, a typical air conditioning load is modeled with the intent of analyzing the interaction between electricity generation and consumption.

Although several variables, such as temperature, solar radiation, humidity, wind speed, and air infiltration, influence the flow and storage of heat in a very complex manner [45], the primary concern of this thesis is to simply generate a power profile representing the behavior of an air conditioning load. The circuit model of an air conditioning load is developed using a dc voltage source in series with a switch and a resistor, as shown in Fig. 7.

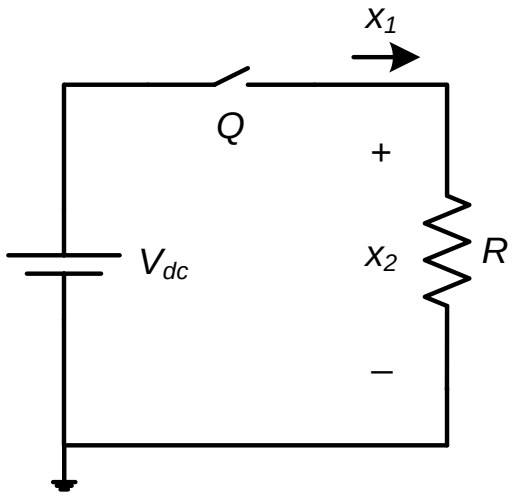

Figure 7: Circuit model of air conditioning load

With x_1 and x_2 signifying the operating current and operating voltage, respectively, of the air conditioner, and $q(t)$ denoting the switching function for Q, the equations in (2.11) are derived. When switch Q is closed ($q(t) = 1$), the operating voltage is equal to V_{dc}, which means that the air conditioner is on and consuming power. On the contrary, an open switch ($q(t) = 0$) indicates that the air conditioner is off and not consuming any power.

$$\begin{cases} x_1 = \dfrac{q(t) \cdot V_{dc}}{R} \\ x_2 = q(t) \cdot V_{dc} \end{cases} \tag{2.11}$$

Thus, the power consumed by the air conditioner can be expressed as:

$$P = x_1 \cdot x_2 \tag{2.12}$$

2.4 ENERGY STORAGE

In addition to developing models that pertain to the supply and consumption of electricity, the storage of electrical energy in a modernized grid is a notable feature whose modeling must also be addressed. Integration of energy storage in a distribution network improves the availability of energy, especially in a network characterized by generation units with non-deterministic sources such as solar and wind. Not only can the presence of energy storage compensate for the uncertainty in such sources, but it can also make power dispatching and load leveling more manageable. With the aid of distributed storage, energy can be stored when the source is abundant and demand is low, and later be harnessed during periods of peak demand.

Modeling energy storage provides an understanding of how home load profiles will be influenced in meeting constant demand. In particular, homes equipped with PV generation or electrical vehicles will be subject of investigation, as the impact of energy storage will undoubtedly influence system performances. Various technologies, such as thermal storage, batteries, and ultracapacitors, may be employed depending on requirements of the specific application for which they are intended. In this thesis, the modeling of lead acid batteries is considered.

Although limited by their cycling capability, lead acid batteries provide high energy densities and technological maturity. For the sake of simplicity, the model developed in this thesis makes several assumptions that may be amended in future work. However, the developed model is adequate enough in providing a foundation for analysis.

In practice, the dynamic characteristics of a battery depend on the state of charge, charge/discharge rate, and temperature [50]. However, these facets are neglected in the realization of the model developed here. Additionally, the effects of overcharging and deep discharging, which may lead to premature failure of the battery, are also not considered in this model. Unlike the more sophisticated and accurate models developed in [51]-[53], the model proposed in this thesis is simplistic in that it uses a series connection of an ideal voltage source

and a resistor. However, such a model suggests a linear operating behavior, which is untrue of most battery technologies. Other parameters that will not be taken into consideration are overvoltage effects and the self-discharge of the battery, particularly at the bottom 20% of the state of charge.

Distributed energy storage can be viewed both as a consumer and producer of power, and thus participates in the market as both a load and generator [54]; therefore, the modeling in this thesis considers both the charging and discharging modes of a lead acid battery.

2.4.1 Charging of Lead Acid Battery

The circuit model for the charging mode of a lead acid battery is shown in Fig. 8, where $\mathcal{E}$ is an ideal voltage source also known as the electromotive force (emf), r is the internal resistance, x_1 is the charging current, and x_2 is the charging voltage.

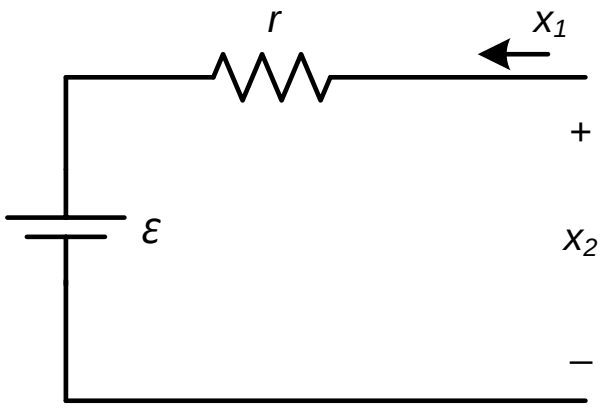

Figure 8: Circuit model of lead acid battery during charging mode

A battery's state of charge relates the percentage of power available compared to its full capacity. The capacity, typically defined in ampere-hours, conveys both the amount and duration of power that can be supplied or extracted by the battery. By knowing what the capacity and charging voltage of the battery are, the current carrying capability of the battery can be

designated via the internal resistance and state of charge. Specifically, the internal resistance determines the amount of current, while the state of charge determines the duration the current is to be carried until the battery is either charged or depleted to a subsequent state of charge. So, with a known charging voltage x_2, the model in Fig. 8 becomes a closed circuit whose current x_1 can be expressed as

$$x_1 = \frac{x_2}{r} \tag{2.13}$$

and, it follows that the power consumed by the battery during its charging operation is:

$$P = x_1 \cdot x_2 \tag{2.14}$$

The time t (in hours) required for a battery of capacity B and state of charge S to reach full charge can be calculated by:

$$t = \frac{B - B \cdot S}{x_1} \tag{2.15}$$

2.4.2 Discharging of Lead Acid Battery

The circuit model for the discharging mode of a lead acid battery is shown in Fig. 9. Instead of power being supplied by an external charging voltage as before, the emf supplies power to the load, which is represented by resistance R_{load}. Therefore, the direction of the discharging current x_1 is reversed in comparison to the charging mode, and is expressed as:

$$x_1 = \frac{\varepsilon}{r + R_{load}} \tag{2.16}$$

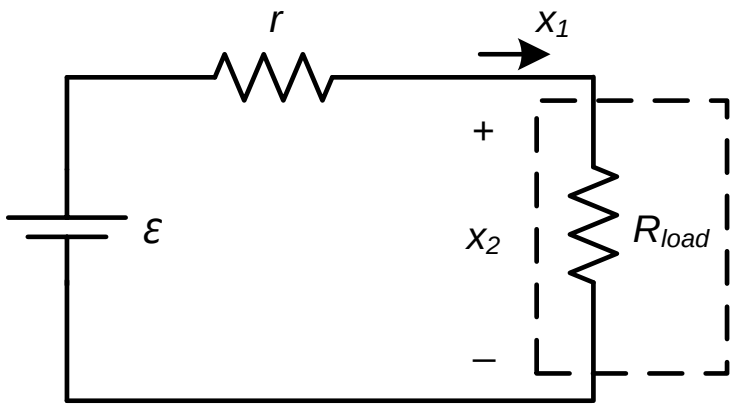

Figure 9: Circuit model of lead acid battery during discharging mode

By knowing the battery's emf and load resistance R_{load}, the discharging current x_1 can be set by fixing the internal resistance r. The discharging voltage x_2 is obtained by finding the difference between the battery's emf and voltage drop across r, according to:

$$x_2 = \varepsilon - x_1 \cdot r \tag{2.17}$$

Thus, the power generated by the discharging of the battery is derived as:

$$P = x_1 \cdot x_2 \tag{2.18}$$

Similar to the charging behavior of the lead acid battery, the period of discharge is determined from the state of charge and battery capacity. The time t (in hours) required for a battery of capacity B and state of charge S to reach full discharge can be calculated by:

$$t = \frac{B \cdot S}{x_1} \tag{2.19}$$

2.5 CONDUCTORS

Conductors, which refer to any transmission line or cable that carries current, are necessary for transmitting power from one component to another. In this thesis, conductors with relatively short distances are considered, hence implying that their capacitance and conductance are ignored. Moreover, both ac and dc conductor models are addressed, since some components operate with ac power while others operate with dc power.

2.5.1 ac Conductor

The equivalent circuit model of a short ac transmission line is shown in Fig. 10, where the conductor or line is represented by the lumped parameters R_{line} and L_{line}. The two ends of the line are referred to as the sending end and receiving end, which correspond to the source side and load side, respectively. R_{line} is the resistance and L_{line} is the inductance of the entire line, x_1 is the line current, V_{ac} is the sending end voltage, and x_2 is the receiving end voltage. The transmission of electricity in a conductor results in energy waste referred to as line loss. These losses occur as a result of electricity being converted to heat and electromagnetic energy.

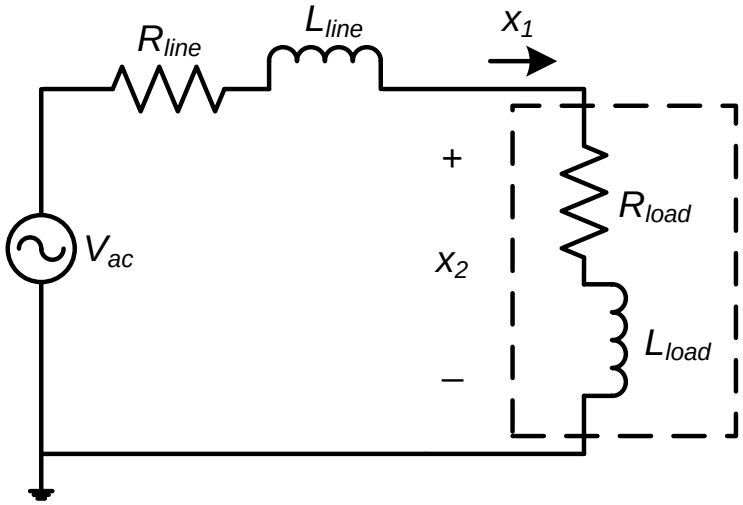

Figure 10: Circuit model of ac conductor

R_{load} and L_{load} represent the resistive and inductive components, respectively, of the collective equivalent load connected to the receiving end of the line, and they allow current x_1 to flow by closing the circuit. The dynamic equations of an ac conductor are derived as follows:

$$\begin{cases} \dot{x}_1 = \dfrac{V_{ac} - R_{line} \cdot x_1 - R_{load} \cdot x_1}{L_{line} + L_{load}} \\ x_2 = V_{ac} - R_{line} \cdot x_1 - L_{line} \dot{x}_1 \end{cases} \tag{2.20}$$

And, the line loss P_{line} is calculated as:

$$P_{line} = R_{line} \cdot (x_1)^2 \tag{2.21}$$

2.5.2 dc Conductor

The equivalent circuit model of a dc conductor is shown in Fig. 11, where the conductor or line is represented by the parameter R_{line}, and the load is represented by the parameter R_{load}. In a dc steady state condition, both the line inductance and load inductance are zero; therefore, only the resistances are taken into account.

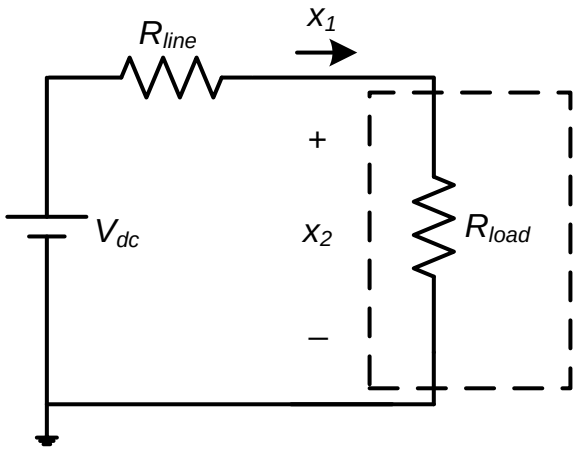

Figure 11: Circuit model of dc conductor

Furthermore, V_{dc} and x_2 denote the sending end voltage and receiving end voltage, respectively. The difference between these voltages results from a voltage drop across R_{line}. The mathematical equations describing a dc conductor are:

$$\begin{cases} x_1 = \dfrac{V_{dc}}{R_{line} + R_{load}} \\ x_2 = V_{dc} - R_{line} \cdot x_1 \end{cases} \tag{2.22}$$

And, the line loss P_{loss} is calculated as:

$$P_{loss} = R_{line} \cdot (x_1)^2 \tag{2.23}$$

2.6 PLUG-IN ELECTRIC VEHICLE

Plug-in electric vehicle (PEV) charging, whether controlled or uncontrolled, is expected to have a significant impact on distribution network operation, especially with increasing penetration levels of PEVs. The charging of PEVs increases peak demand, which results in larger voltage drops and a higher probability of transformer overloading [55]. Since aggravating peak demand adversely affects the grid, charging during off-peak hours will be encouraged so that the impact to the system is minimized. This can be accomplished through the use of smart metering systems and real-time pricing information that would jointly allow for an automated charging scheme.

PEVs present several advantages and contribute to a smart grid by serving as a source of dispatchable load, providing generation capabilities via vehicle-to-grid technologies, and reducing fuel costs. Furthermore, driving on electricity is considered less expensive per mile and typically produces less emission than a conventional vehicle [56]. The adoption and utilization of PEVs is particularly appealing given the already existing charging infrastructure in the form of 120/240 V outlets. Regarding charging methods for PEVs, several standards have been explored involving both ac charging and dc charging. Specifically, 'level 1 charging' is defined as single phase 120 Vac with 20 A maximum current, 'level 2 charging' is defined as single phase 240 Vac with 80 A maximum current, and 'level 3 charging' is defined as 500 Vdc maximum voltage with 200 A maximum current [57]. In this thesis, ac charging from the grid will be considered for modeling and simulation. Although fleets of PEVs can present a dichotomy in utilization—they can operate either as energy sources when required by the System Operator, or as loads, during strategic hours of the day when their batteries need to be charged [58]—this thesis is only concerned with the charging of PEVs, i.e., their treatment as loads.

In order for a PEV's battery to be charged from the grid, electricity must be converted from ac to dc by means of a rectifier, whose modeling and operation will be discussed later in this thesis. An equivalent circuit model of a PEV during its charging operation is developed in Fig. 12, where V_{ac} is the charging voltage supplied from the grid, I_{ac} is the charging current from

the grid's perspective, x_1 is the charging current from the rectifier's perspective, x_2 is the charging voltage from the rectifier's perspective, and $R_{battery}$ is the resistance representing the PEV's battery. V_{ac} and x_2 are related by an efficiency factor of η_v, and I_{ac} and x_1 are related by an efficiency factor of η_i, such that the rectifier's overall efficiency is given by:

$$\eta = \eta_v \cdot \eta_i \tag{2.24}$$

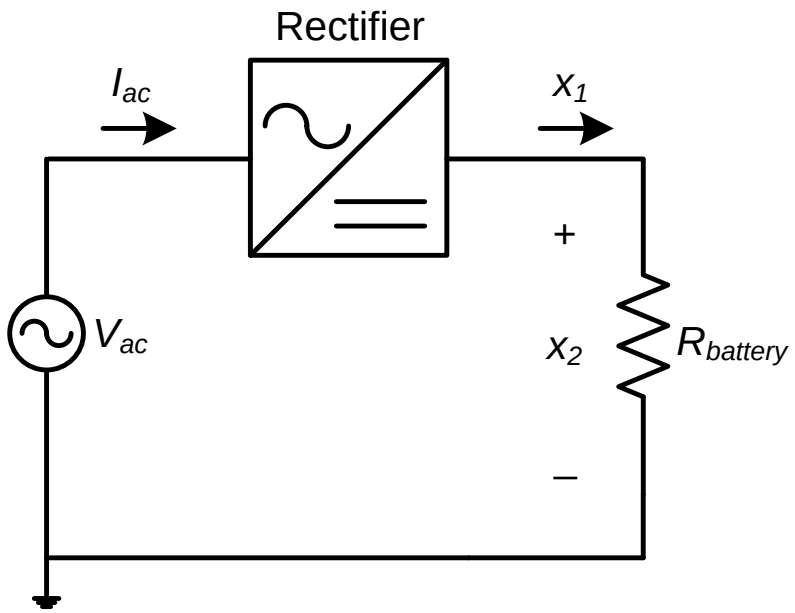

Figure 12: Circuit model of a PEV when charged from the grid

Given that the charging voltage V_{ac} is user-defined, i.e., it is known, the following equations can be obtained for describing the circuit model in Fig. 12:

$$\begin{cases} x_1 = \dfrac{x_2}{R_{battery}} \\ x_2 = \eta_v \cdot V_{ac} \cdot \sqrt{2} \end{cases} \tag{2.25}$$

It is important to note that (2.25) relates the current and voltage from the rectifier's perspective; however, the analysis in this thesis follows a trend, in that the impact of components is observed from the perspective of the grid. Therefore, in keeping consistent with this practice, the charging current I_{ac} from the grid's perspective is derived according to:

$$I_{ac} = \frac{x_1 \cdot \sqrt{2}}{\eta_i} \tag{2.26}$$

Using the conservation of power principle, the power consumed from the grid during the charging of the PEV is calculated by:

$$P = \frac{x_1 \cdot x_2}{\eta} \tag{2.27}$$

Given the PEV's battery capacity B and state of charge S, the time t in (in hours) required for the battery to reach full charge is:

$$t = \frac{B - B \cdot S}{x_1} \tag{2.28}$$

2.7 POWER ELECTRONICS INTERFACE

Power electronics play a crucial role in interfacing and integrating the various components of a smart grid. In a grid characterized by an active two-way flow of power, power electronic converters would be essential in driving and controlling the energy storage unit, e.g., a dc-dc bi-directional converter for connecting the battery to a dc link. With power electronics, unwanted harmonics in the power system can be filtered, voltage levels can be adjusted to suit different applications, and dc power can be converted to ac power or vice versa. Furthermore, the connection of distributed generation units through power electronic interfaces provides additional services, such as reactive power support, load following, back-up service, peak shaving, and power quality disturbance compensation, all of which contribute to the satisfactory operation of the network [59]. It is therefore valid to assert that, without power electronic devices, the sophisticated delivery of electric power from the sub-transmission system to the end user's meter is not realizable. This thesis addresses dc-dc converters, namely the buck converter and boost converter, as well as the ac-dc rectifier, and the dc-ac inverter.

2.7.1 Buck Converter

Before the advent of dc-dc converters, power was manipulated by obtaining energy from an ac line source, changing its level with a transformer, then rectifying the result. With dc-dc converters, however, the incoming ac is directly rectified, and then the high-level dc is converted to the desired level. dc-dc converters such as the buck converter or boost converter serve in many important applications where energy is transferred between two dc circuits operating at different voltage and current levels. In fact, many products are designed around 170 V inputs (the peak value of rectified 120 Vac) or 300-400 V inputs (the peak values of 230 Vac, 240 Vac, and many three-phase rectified sources) [60]. These converters operate by temporarily storing the input energy, either by means of magnetic field storage components or electric field storage components, and then releasing it to the output at a different voltage.

The circuit model of a buck converter, which uses two switches (MOSFET Q and diode Q_D), an inductor L, and a capacitor C, is shown in Fig. 13. This converter operates by alternating between two states: storing energy in the inductor by connecting it to the source voltage, or discharging the inductor into the load by disconnecting it from the source voltage. During the interval when the switch is on, the diode becomes reverse biased, and the input supplies energy to the load as well as to the inductor. During the interval when the switch is off, the inductor current x_1 flows through the diode and transfers some of its stored energy to the load [61].

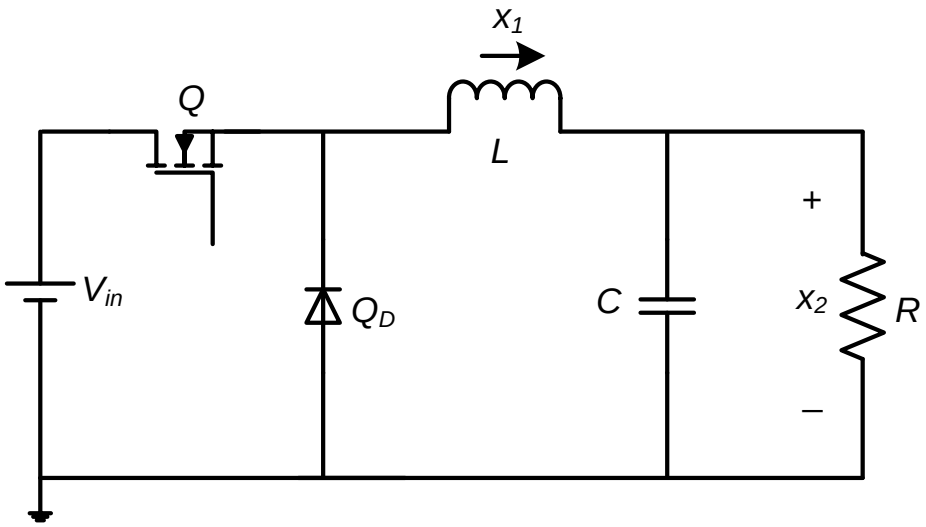

Figure 13: Circuit model of a buck converter

The buck converter produces a lower average output voltage x_2 than the dc input voltage V_{in}, because x_2 is multiplied by a scalar factor, smaller than unity, at the output [62]. Assuming the converter is in continuous conduction mode, i.e., the inductor current x_1 never reaches zero during the commutation cycle, the input-output voltage relationship is

$$x_2 = V_{in} \cdot D \tag{2.29}$$

where D denotes the duty cycle, or average control input of Q. The dynamic equations of the converter are described by

$$\begin{cases} \dot{x}_1 = \dfrac{1}{L} \cdot \left(DV_{in} - x_2 \right) \\ \dot{x}_2 = \dfrac{1}{C} \cdot \left(x_1 - \dfrac{x_2}{R} \right) \end{cases} \tag{2.30}$$

and the output power is obtained according to:

$$P_{out} = x_2 \cdot \left(x_1 - C\dot{x}_2 \right) = \frac{\left(x_2 \right)^2}{R} \tag{2.31}$$

2.7.2 Boost Converter

The boost converter, whose circuit model is shown in Fig. 14, is another type of dc-dc converter. This converter produces a higher output voltage x_2 in relation to its input voltage V_{in}. When switch Q is on, the output stage is isolated because diode Q_D is reverse biased; therefore, inductor L is charged during this interval. When the switch is off, the output stage receives energy from both the inductor and the input. Filter capacitor C is added to the output to reduce the output voltage ripple. Assuming the converter is in continuous conduction mode, the input-output voltage relationship is as follows:

$$x_2 = \frac{V_{in}}{1 - D} \tag{2.32}$$

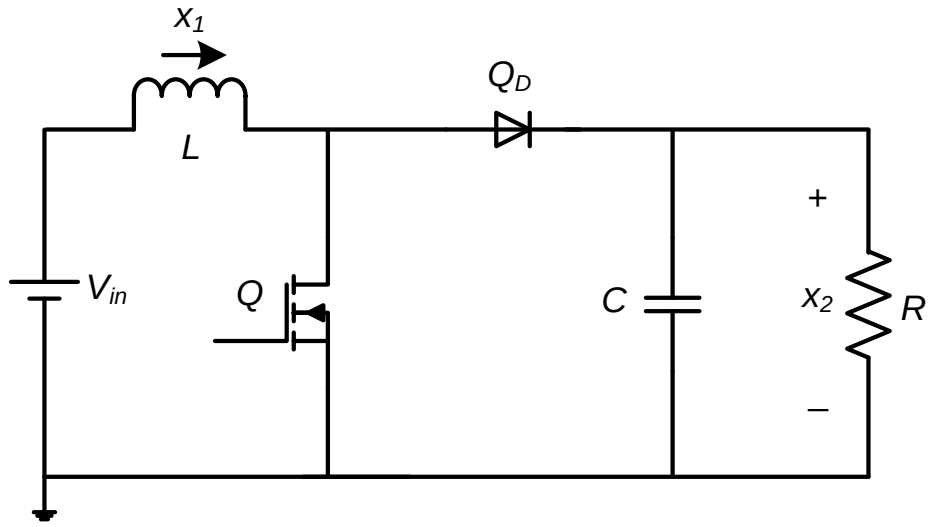

Figure 14: Circuit model of a boost converter

Denoting the inductor current and capacitor voltage by x_1 and x_2, respectively, the dynamic equations of the boost converter can be obtained as

$$\begin{cases} \dot{x}_1 = \dfrac{1}{L} \cdot \left(V_{in} - \left[\left(1-D\right) \cdot x_2\right]\right) \\ \dot{x}_2 = \dfrac{1}{C} \cdot \left(\left[\left(1-D\right) \cdot x_1\right] - \dfrac{x_2}{R}\right) \end{cases} \tag{2.33}$$

and the output power is derived according to:

$$P_{out} = x_2 \cdot \left[\left(1-D\right) \cdot x_1 - C\dot{x}_2\right] = \frac{\left(x_2\right)^2}{R} \tag{2.34}$$

2.7.3 Rectifier

Power electronic devices that convert ac to dc are referred to as rectifiers. The model developed here is that of a single-phase full-wave rectifier, which converts the whole of the input waveform to one of constant polarity at the output. The single-phase rectifier can be used since the grid model is reduced to the single-phase equivalent. The topology, shown in Fig. 15, uses four diodes that rectify the incoming voltage V_{ac}. The inductor L serves to improve the line-current waveform, while the output capacitor C exists to smooth the peak-to-peak ripple voltage in x_2 to a reasonable value.

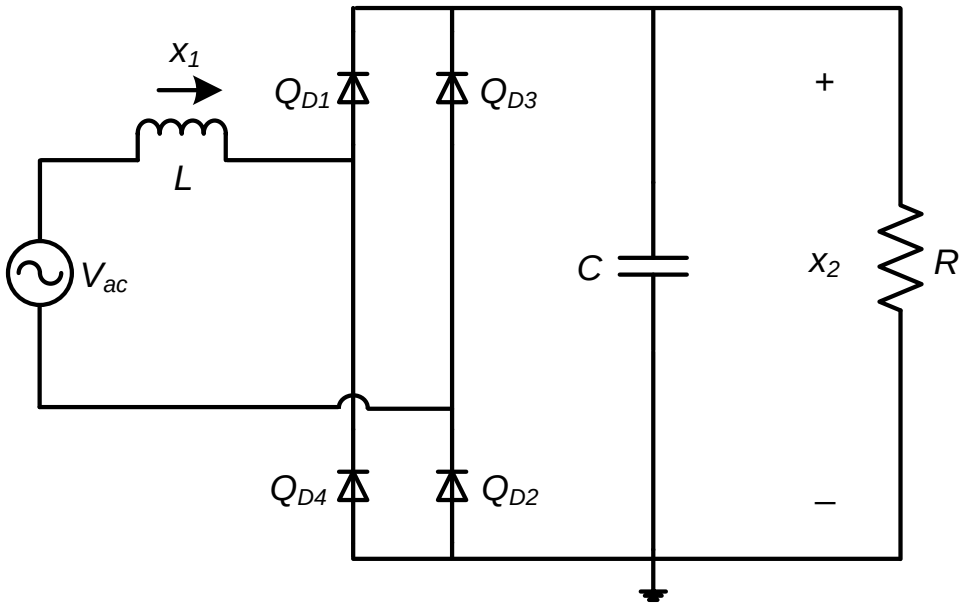

Figure 15: Circuit model of a rectifier

The rectifier operates by having alternating pairs of diodes conduct during each alternating half-cycle of V_{ac}. When V_{ac} is positive, only Q_{D1} and Q_{D2} conduct current since V_{ac} appears as a reverse-bias voltage across Q_{D3} and Q_{D4}. When V_{ac} is negative, the current commutates to Q_{D3} and Q_{D4}, and a reverse-bias voltage appears across Q_{D1} and Q_{D2}. This operating behavior can

equivalently be described by the circuit model in Fig. 16, where the absolute value of the input voltage V_{ac} represents the effect of the diodes.

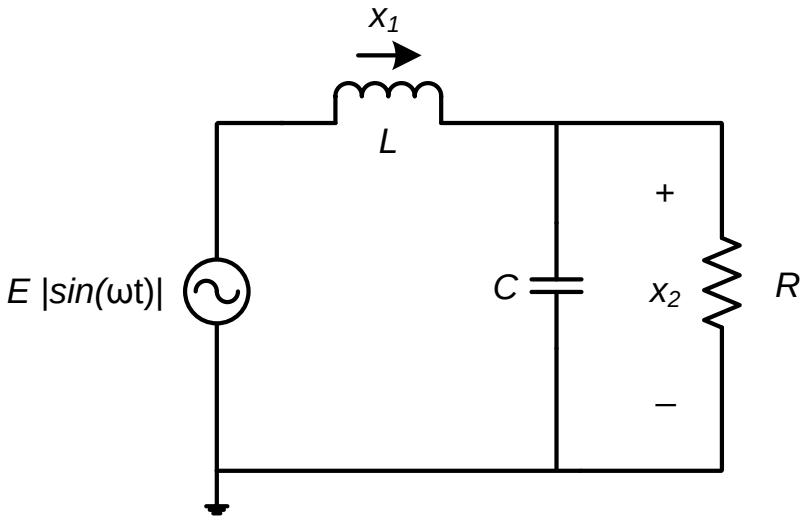

Figure 16: Equivalent-circuit model of Fig. 15

Using the above representation, the dynamic equations of the rectifier can be obtained as

$$\begin{cases} \dot{x}_1 = \dfrac{1}{L} \cdot \left(E\left|\sin(\omega t)\right| - x_2 \right) \\ \dot{x}_2 = \dfrac{1}{C} \cdot \left(x_1 - \dfrac{x_2}{R} \right) \end{cases} \tag{2.35}$$

where E is the amplitude of V_{ac}, x_1 is the inductor current, and x_2 is the capacitor voltage. Consequently, the output power is given by:

$$P_{out} = x_2 \cdot \left(x_1 - C\dot{x}_2 \right) = \frac{\left(x_2\right)^2}{R} \tag{2.36}$$

2.7.4 Inverter

Another power electronics interface relevant within the realm of a smart grid is the inverter, which converts dc to ac. Such a device is often used to connect a dc bus to the ac grid, particularly in applications involving PV plants or wind plants. PWM (pulse width modulation) schemes are typically implemented in the switching strategy to shape the output ac voltage as close to a sine wave as possible. The model of a single-phase H-bridge inverter with unipolar PWM implementation is considered in this thesis.

The topology of a single-phase H-bridge inverter is shown in Fig. 17, where V_{dc} is the input dc voltage, L_{filter} and C_{filter} denote the filter inductor and filter capacitor, respectively, R_{load} is the load resistance, x_1 is the inductor current, x_2 is the capacitor voltage, and switches Q_{11}, Q_{12}, Q_{21}, Q_{22} strategically operate via PWM in generating an ac output.

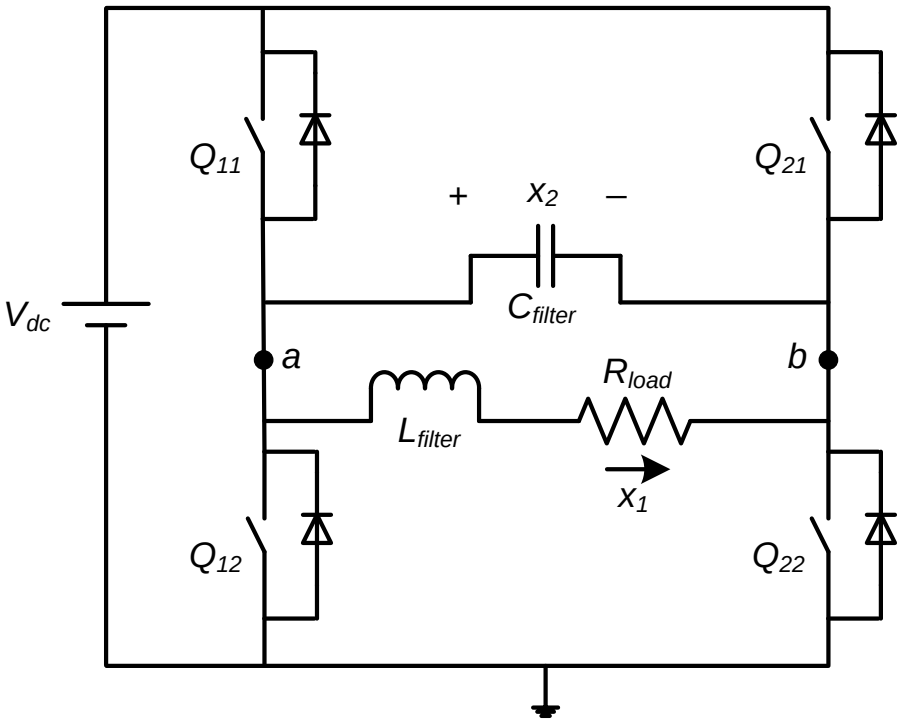

Figure 17: Circuit model of a single-phase H-bridge inverter

The switching action of the inverter produces harmonics, which are sine waves with frequencies that are integral multiples of the fundamental frequency. Therefore, a filter is applied to the inverter to permit the fundamental component of the waveform to pass to the output while restricting the passage of harmonic components. In order to generate the switching signals for Q_{11}, Q_{12}, Q_{21}, and Q_{22}, two control signals, v_{cont} and $-v_{cont}$, are compared to a repetitive switching-frequency triangular waveform v_{tri}, as shown in Fig. 18. The switching scheme is as follows:

- If $v_{cont} > v_{tri}$, close Q_{11} and open Q_{12}, so $V_a = V_{dc}$
- If $v_{cont} < v_{tri}$, open Q_{11} and close Q_{12}, so $V_a = 0$
- If $-v_{cont} > v_{tri}$, close Q_{21} and open Q_{22}, so $V_b = V_{dc}$
- If $-v_{cont} < v_{tri}$, open Q_{21} and close Q_{22}, so $V_b = 0$

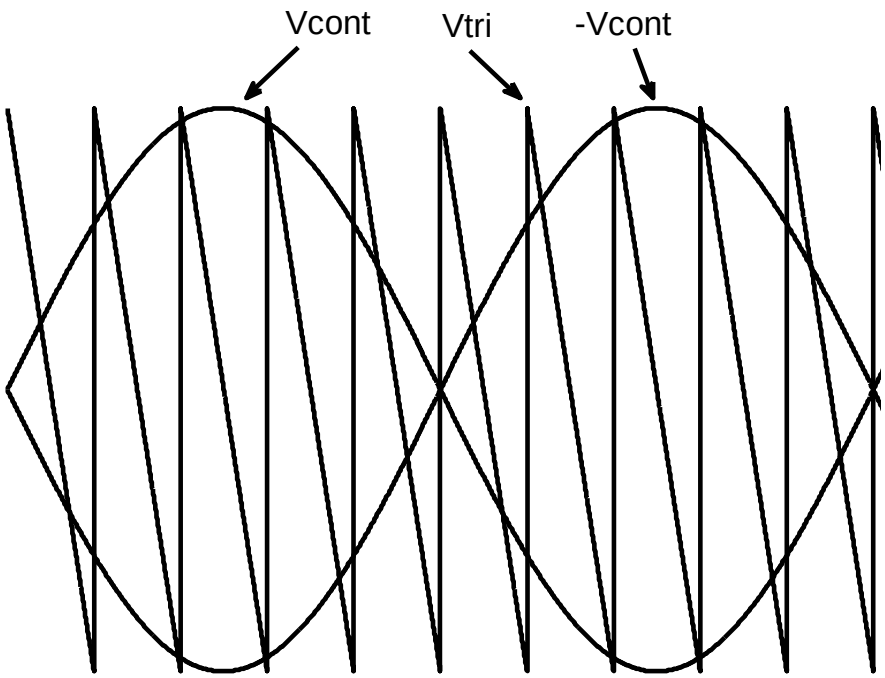

Figure 18: Comparison of v_{cont} and $-v_{cont}$ with v_{tri}

This type of PWM scheme is known as unipolar voltage switching, because the output voltage changes between zero and $+V_{dc}$ or between zero and $-V_{dc}$ voltage levels. To illustrate, Fig. 19 represents a conceptual load voltage waveform, which is the equivalent of $V_a - V_b$ in the circuit model of Fig. 17.

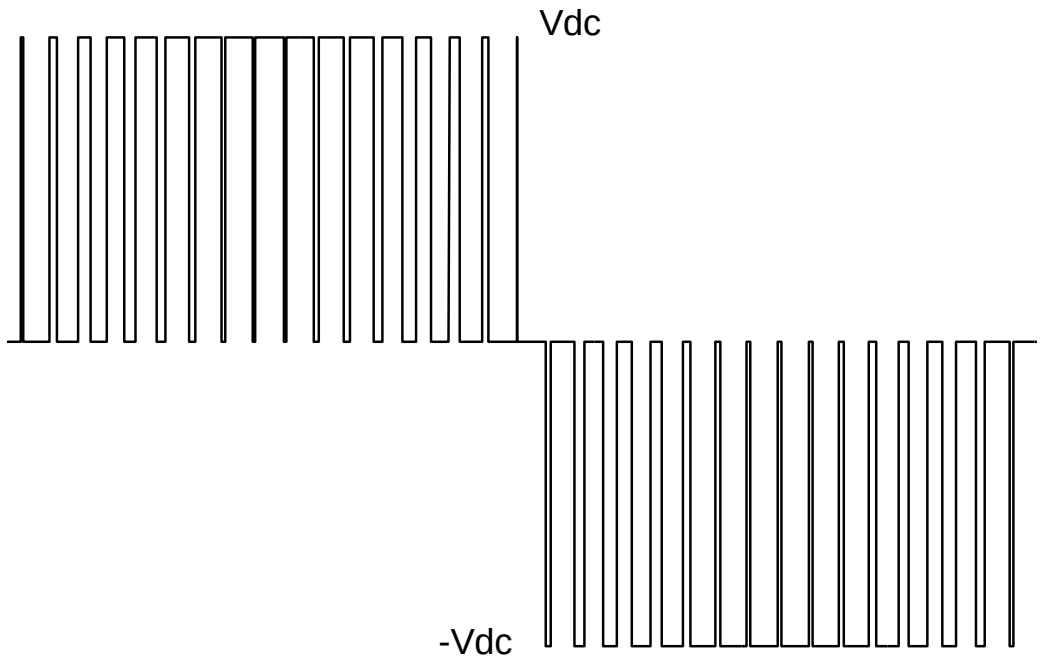

Figure 19: Load voltage with unipolar PWM

The switching frequency of the triangle wave, which is generally kept constant, establishes the inverter switching frequency. Meanwhile, the frequency of the control signal is the desired fundamental frequency of the inverter voltage output. Hence, v_{cont} is used to modulate the switch duty ratio, and the ratio of its amplitude to the amplitude of v_{tri} (generally kept constant) signifies the amplitude modulation ratio m_a. Similarly, a frequency modulation ratio m_f is defined as the ratio of the triangle wave frequency to the control signal frequency.

Referring to Fig. 17, the equations describing the output of the inverter are

$$\begin{cases} \dot{x}_1 = \dfrac{x_2 - R_{load} x_1}{L_{filter}} \\ x_2 = V_a - V_b \end{cases} \tag{2.37}$$

and the output power of the inverter is described by:

$$P_{out} = x_1 \cdot \left(x_2 - L_{filter} \dot{x}_1\right) = R_{load} \cdot \left(x_1\right)^2 \tag{2.38}$$

Chapter 3: Simulation of Components

Using the equations developed earlier, the proposed models are investigated in this chapter by creating blocks in MATLAB/Simulink. The blocks will prompt the user to provide certain information necessary to perform simulations that convey the power generation/consumption of these components.

3.1 PHOTOVOLTAIC ARRAY

The PV array block shown in Fig. 20 is developed using (2.7). The parameters in Table 1, obtained from a Kyocera KC200GT datasheet [63], are considered for simulating the model. Additionally, the values in Table 2 relate the ambient conditions and specifications of the PV array.

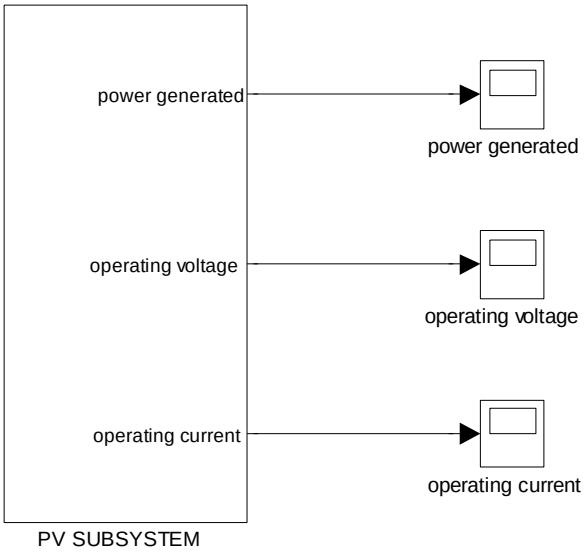

Figure 20: Photovoltaic array block

Nominal short-circuit current, $I_{sc,n}$ [A]	8.21
Nominal open-circuit voltage, $V_{oc,n}$ [V]	32.9
Current at maximum power point, I_{mp} [A]	7.61
Voltage at maximum power point, V_{mp} [V]	26.3
Voltage/temperature coefficient, K_V [V/K]	-0.123
Current/temperature coefficient, K_I [A/K]	0.00318
Number of cells per module, N_s	54

Table 1: Parameters used for simulation of PV model

Nominal irradiation, G_n [W/m^2]	1000
Nominal temperature, T_n [K]	298.15
Actual irradiation, G [W/m^2]	1000
Actual temperature, T [K]	298.15
Number of series modules in array, N_{ss}	5
Number of parallel modules in array, N_{pp}	3

Table 2: Ambient condition and specifications of PV array

The simulation results of the PV array are shown in Figs. 21-23, and they conform to the expected values of an array comprised of 5 series modules and 3 parallel modules, each with a maximum power rating of 200 W. It is observed that the operating voltage of the array is the product of V_{mp} and N_{ss}, whereas the operating current of the array is the product of I_{mp} and N_{pp}. As expected, the power generated by the PV array is approximately 3000 W, and the model is deemed accurate.

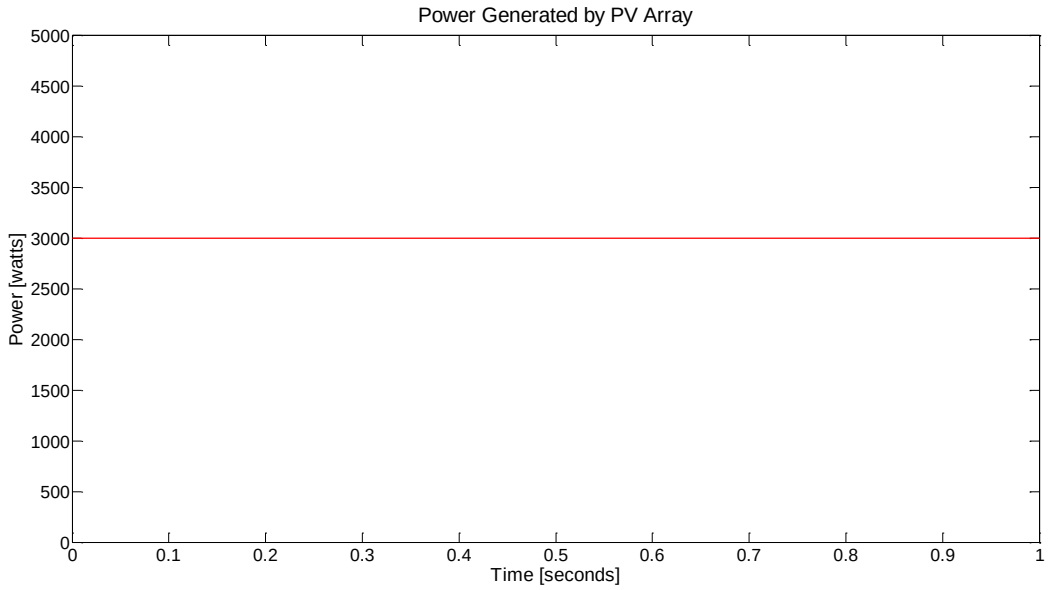

Figure 21: Simulated power generated by PV array

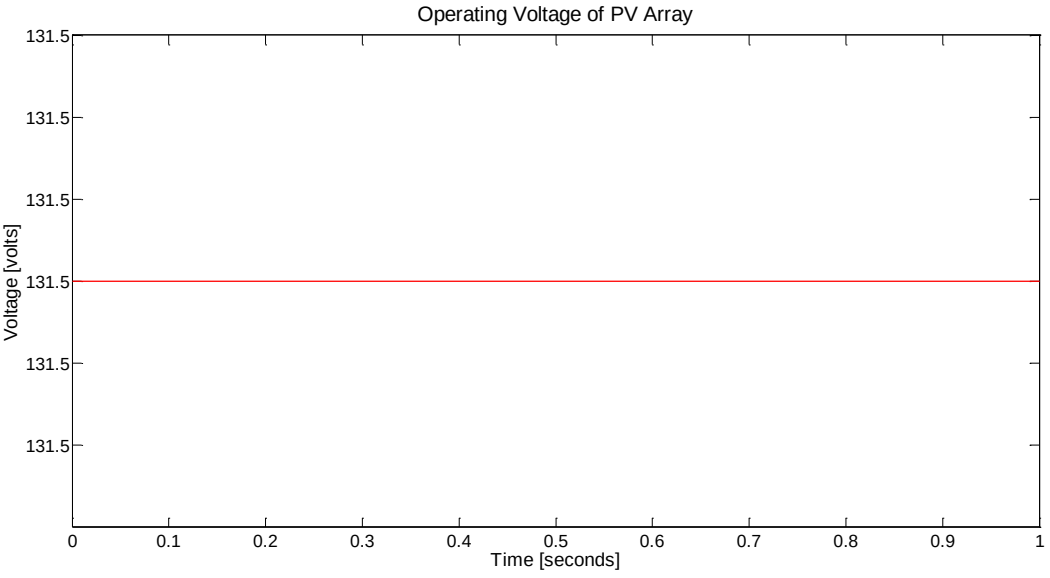

Figure 22: Simulated operating voltage of PV array

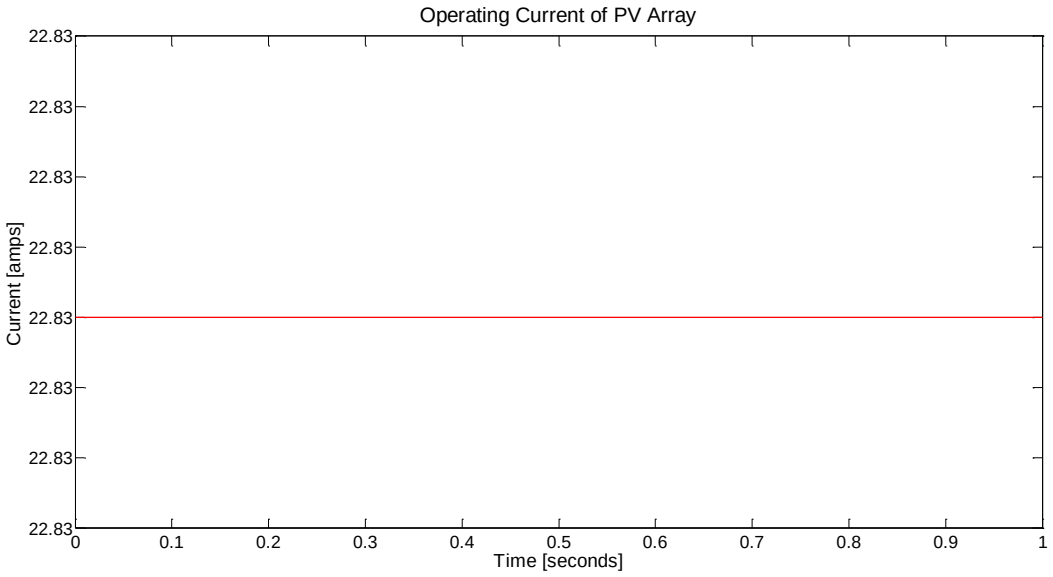

Figure 23: Simulated operating current of PV array

The study of grid-connected PV systems is important because these systems present certain effects at the distribution level that need to be taken into consideration. Power quality issues, in terms of voltage, active power, total losses, and network power factor, influence overall system operation. One study in particular [64], found that PV grid-connected systems can improve the power quality of a distribution feeder. Since PV generators can enhance the distribution operation, they show great potential as a grid support system, whereby voltage profiles are improved and system losses are reduced. Thus, grid-connected PV generation is an enabling technology that fosters a smart grid, as it inherently remedies power quality issues that would otherwise be resolved in a traditional manner, e.g., changing distribution transformer tap ratios or switching on shunt capacitors.

On the contrary, the impacts of PV generation may not always be positive, for the widespread introduction of such generation sources on the distribution system can adversely affect the flow of power and voltage conditions at customer and utility equipment. This may indeed prove to be problematic since distribution systems are generally designed to operate

without any generation on the distribution system or at customer loads [65]. Furthermore, two factors affecting feeder voltage are the size and location of PV generators, and since, in practice, installation locations mainly depend on customers who own the PV systems, utilities are left with limited control regarding this matter. Another reasonable concern is that of voltage dips, which may be caused by clouds passing over an area with large numbers of installed PV systems. Voltage rise poses challenges as well, since any injection of power into a distribution system causes the voltage to rise at the point of connection and in the surrounding network [66], [67].

3.2 ELECTRIC GRID

Using (2.8)-(2.10), the Simulink block in Fig. 24 is created. The parameters in Table 3 are entered into the dialog box shown in Fig. 25.

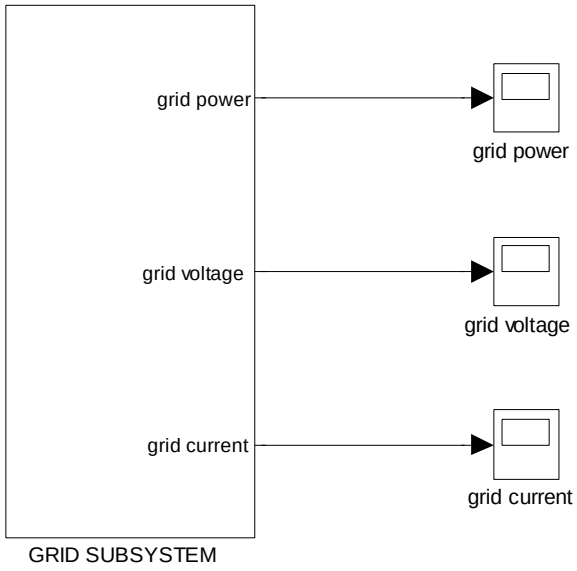

Figure 24: Grid block

Open-circuit voltage [volts ac]	120
Frequency [hertz]	60
Short-circuit inductance [henries]	0.009
Equivalent load-side resistance [ohms]	10
Equivalent load-side inductance [henries]	0.001

Table 3: Parameters used for simulation of grid model

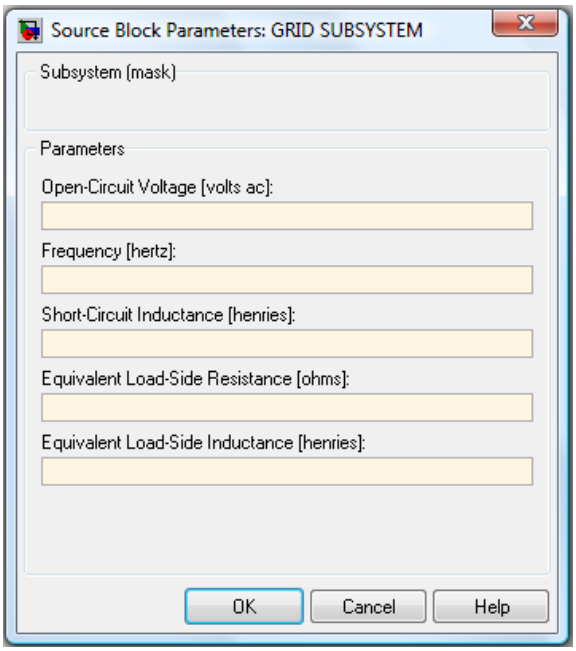

Figure 25: Dialog box for grid model

The simulation results of the grid model are shown in Figs. 26-28. From Fig. 6 in Chapter 2, the grid voltage x_2 represents the voltage at a typical residential outlet socket. This voltage is the difference between the open-circuit voltage V_{ac} and the voltage drop across Z_{eq}. Meanwhile, the grid current is the current that is drawn from an equivalent load connected to the outlet socket. When there is no load, the voltage at the output, x_2, is equal to voltage source V_{ac}; however, when a load is added the circuit becomes closed, allowing current x_1 to flow in Fig. 6. This current results in a voltage drop across Z_{eq}, such that x_2 is no longer equal to V_{ac}. This behavior is evident in Fig. 27, where the simulated grid voltage is less than open-circuit voltage V_{ac} in the presence of a load.

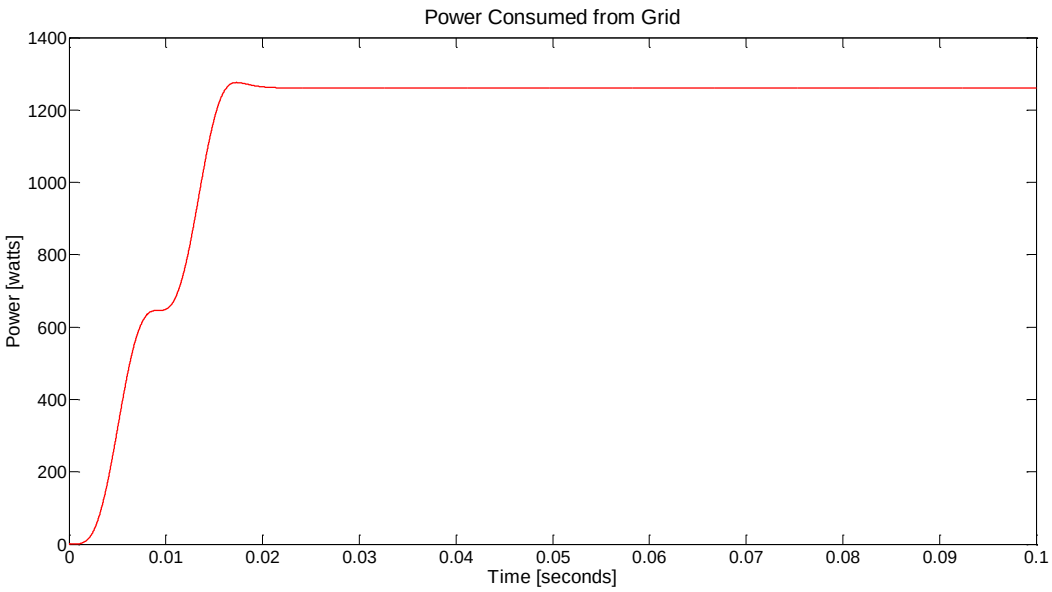

Figure 26: Simulated power consumed from grid

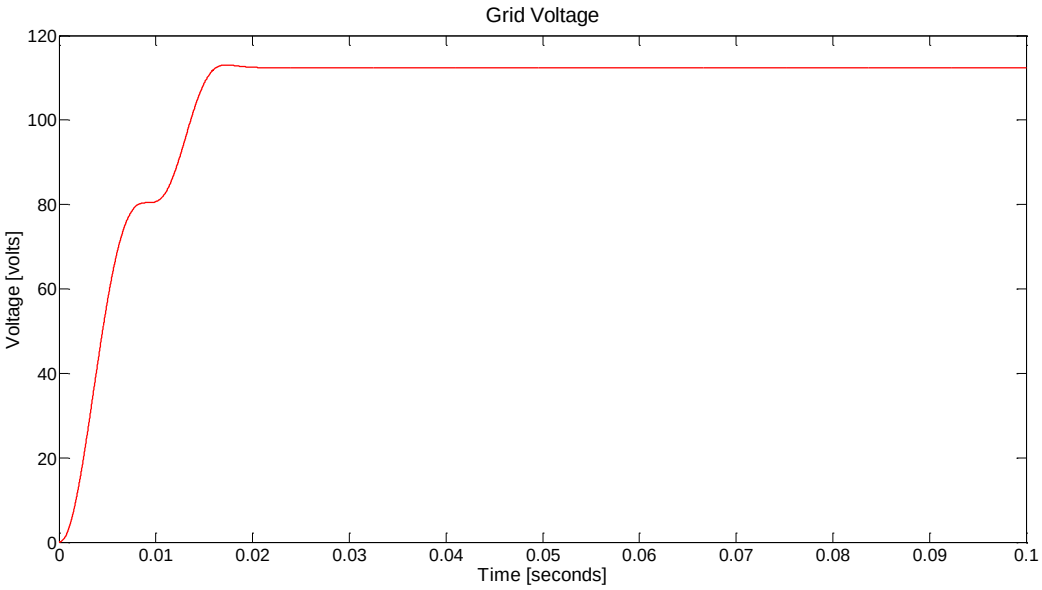

Figure 27: Simulated grid voltage

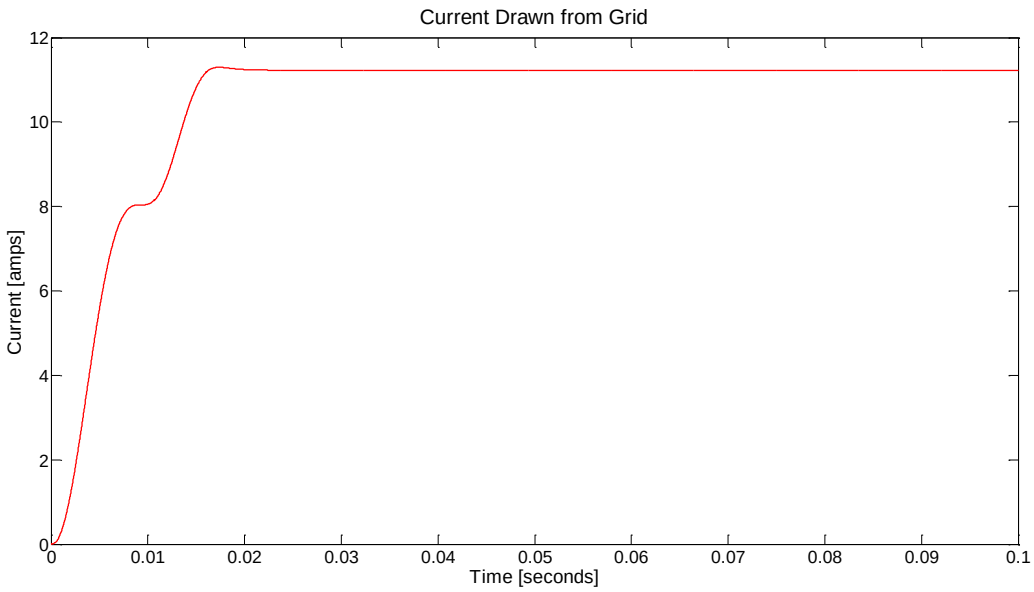

Figure 28: Simulated current drawn from grid

3.3 LOAD

Having derived the necessary equations to model an air conditioning load, the block shown in Fig. 29 is created in Simulink.

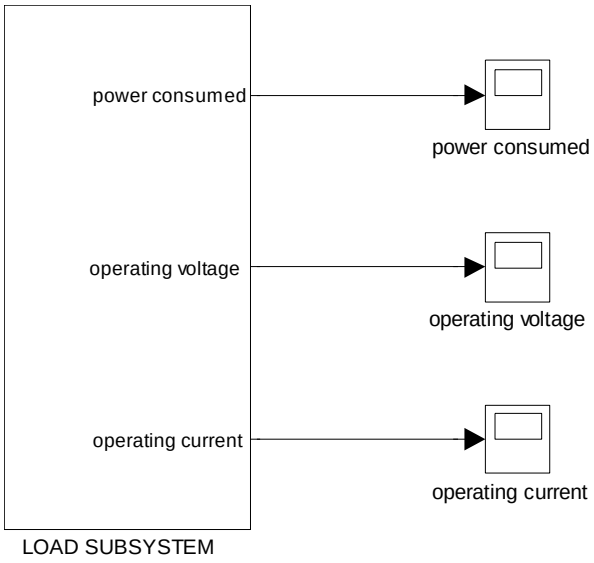

Figure 29: Load block

The dialog box in Fig. 30 requests several parameters necessary for performing the simulation; these parameters and their values are listed in Table 4. The user-defined variables for the simulation include: the power consumed by the load, the duration or period of each on-off cycle, the duty cycle, i.e., the ratio that the load is on within the entire period, and finally, the resistance R corresponding to Fig. 7, which determines the operating voltage and operating current. Setting the simulation time to 3600 seconds, or 1 hour, the model is simulated, and its results are shown in Figs. 31-33.

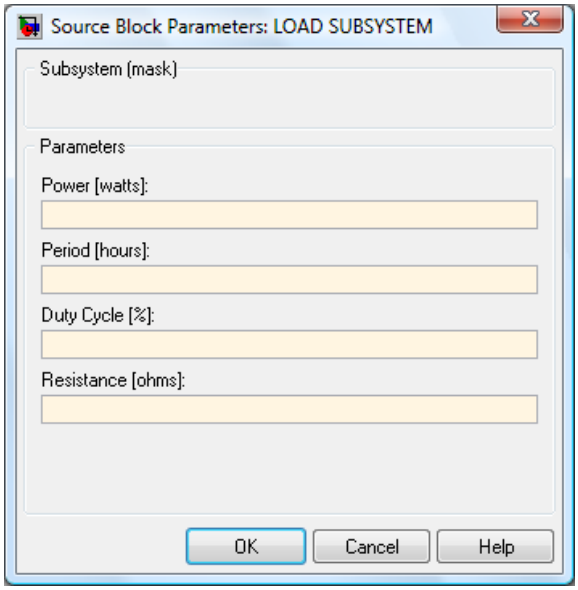

Figure 30: Dialog box for load model

Power [watts]	3200
Period [hours]	1/6
Duty cycle [%]	25
Resistance [ohms]	16

Table 4: Parameters used for simulation of load model

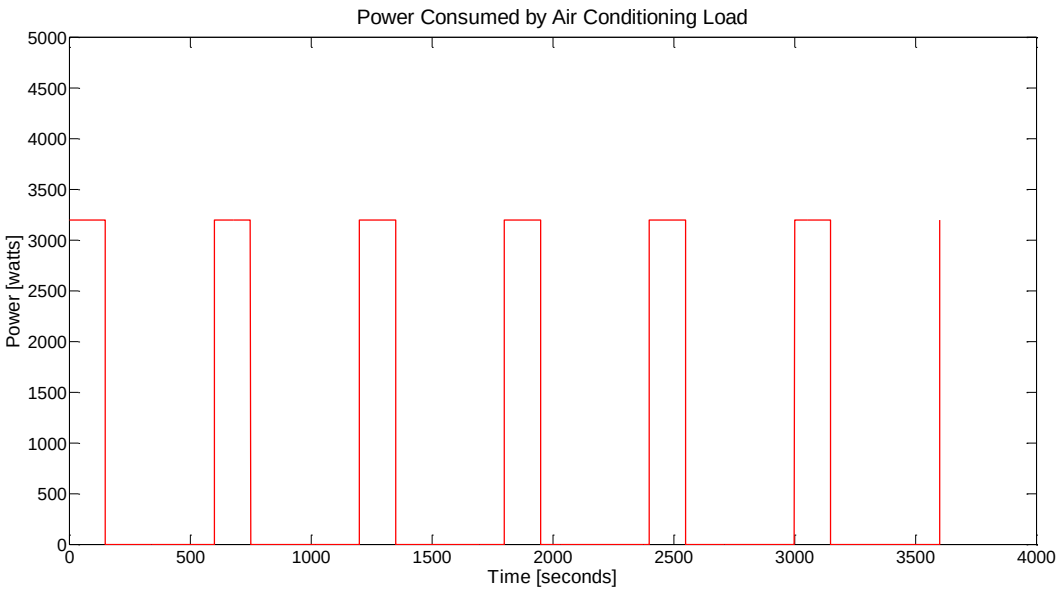

Figure 31: Simulated power consumed by air conditioning load

The power consumption pattern in Fig. 31 resembles the behavior typical of an air conditioning load, as it periodically cycles on and off for a certain amount of time. With the period set to 1/6 of an hour, the duration of each on-off cycle is 600 seconds, or, relating this to frequency, there are 6 total on-off cycles within the entire simulation time of 3600 seconds. A duty cycle of 25% indicates that the load consumes power during 1/4 of each period, i.e., 150 seconds of the 600-second period. In the proceeding figures, Figs. 32 and 33, the operating voltage and operating current of the air conditioning load are depicted. These parameters are dependent upon user-defined values of power consumption and resistance *R* in Fig. 7.

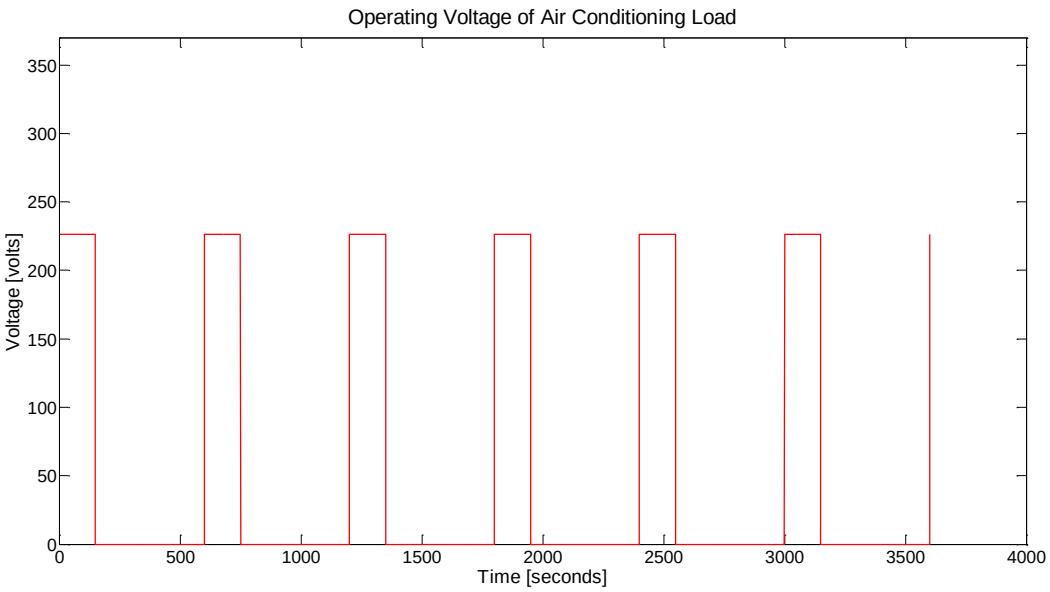

Figure 32: Simulated operating voltage of air conditioning load

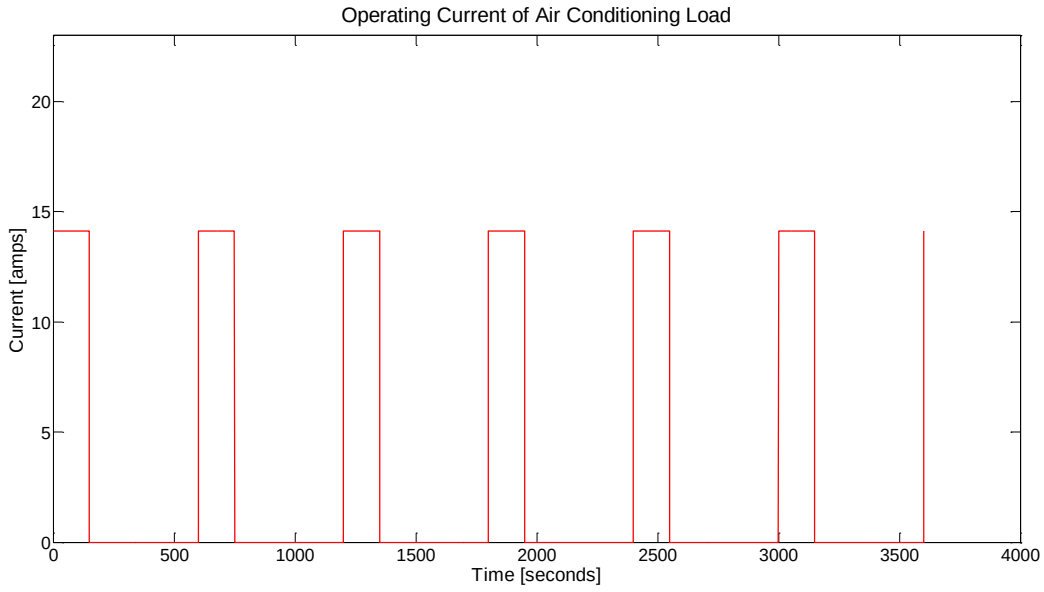

Figure 33: Simulated operating current of air conditioning load

3.4 ENERGY STORAGE

The simulation results of the charging and discharging modes of the battery model are presented.

3.4.1 Charging of Lead Acid Battery

The Simulink block of a lead acid battery model during charging mode is shown in Fig. 34.

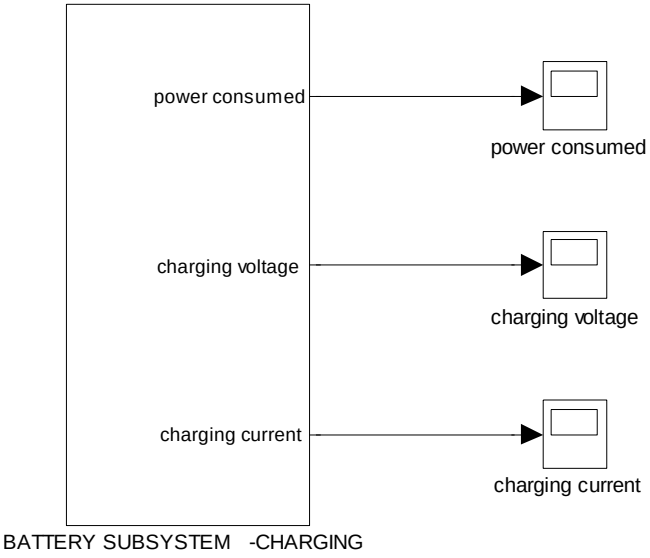

Figure 34: Battery charging block

The dialog box in Fig. 35 shows the user-defined parameters required for the simulation. These parameters and their values are tabulated in Table 5. A battery with capacity of 100 ampere-hours and state of charge of 10% is assumed for the simulation. Knowing that the charging voltage is 200 V, the charging current can be assigned by calculating the internal resistance. In this case if a charging current of 14 A is desired, then the internal resistance would be 14.2857 Ω.

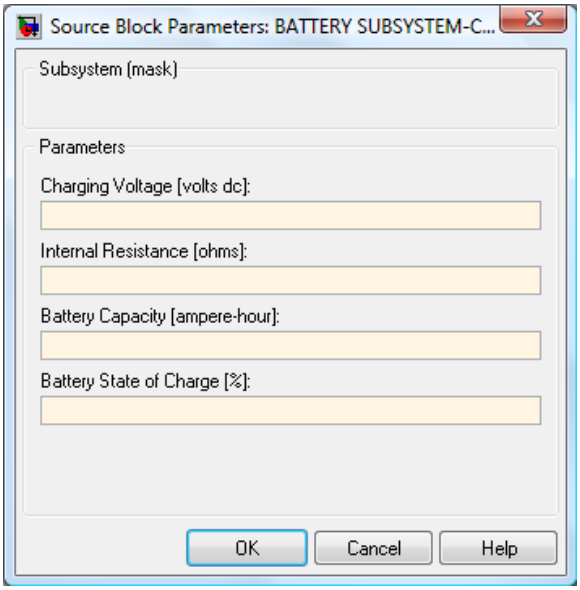

Figure 35: Dialog box for battery charging model

Charging voltage [volts dc]	200
Internal resistance [ohms]	14.3
Battery capacity [ampere-hour]	100
Battery state of charge [%]	10

Table 5: Parameters used for simulation of battery charging model

In Figs. 36-38, simulation results of the battery model during its charging mode are depicted. The simulation is designed to run until the battery is fully charged, i.e., reaches a state of charge of 100%. Applying (2.15), it is observed that the simulation stops after 6.429 hours, or 23143 seconds.

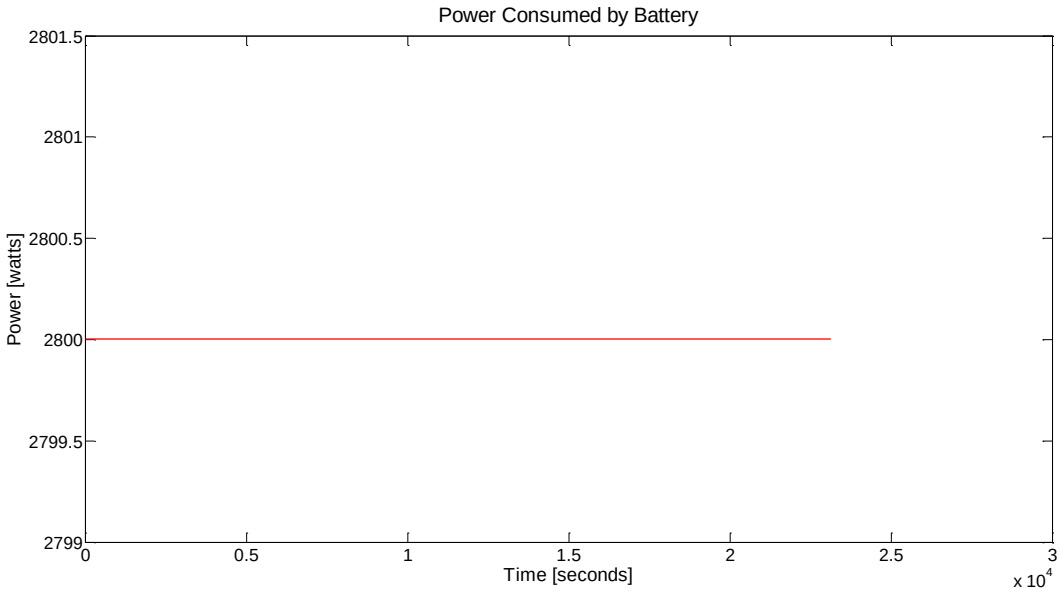

Figure 36: Simulated power consumed by battery

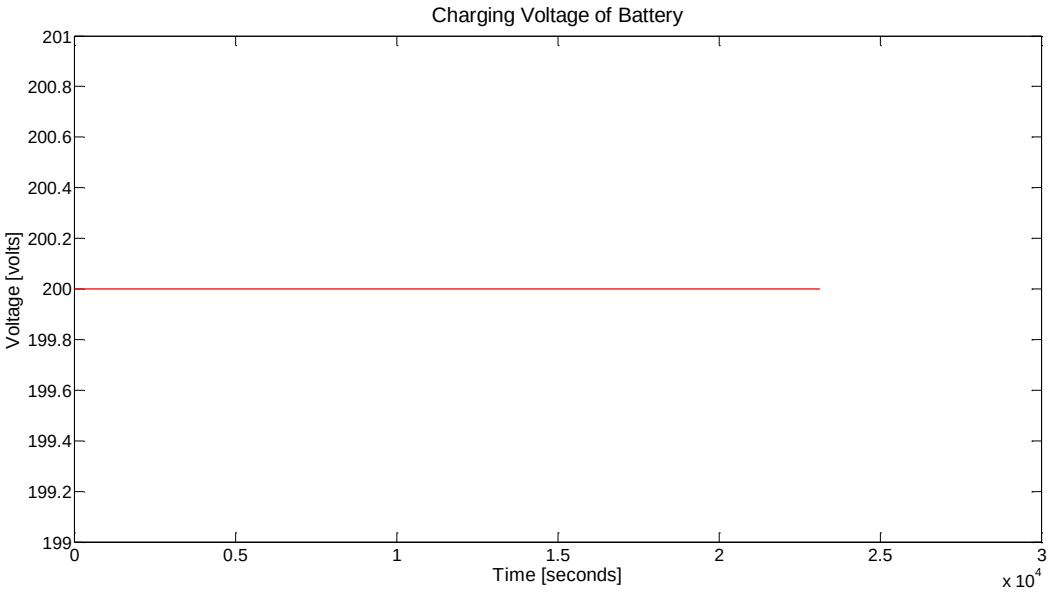

Figure 37: Simulated charging voltage of battery

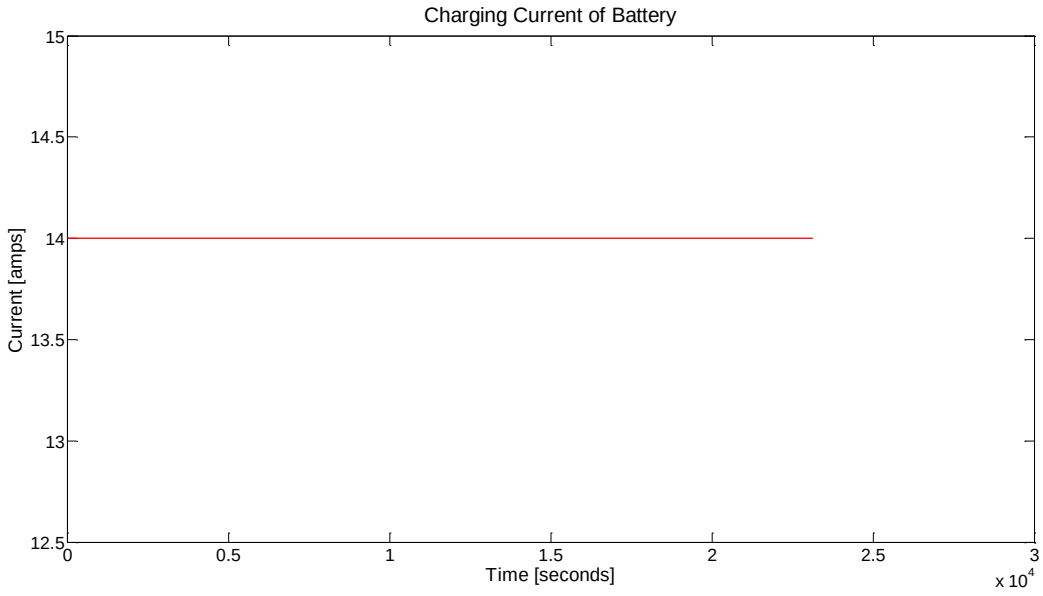

Figure 38: Simulated charging current of battery

3.4.2 Discharging of Lead Acid Battery

The Simulink block of a lead acid battery model during discharging mode is shown in Fig. 39.

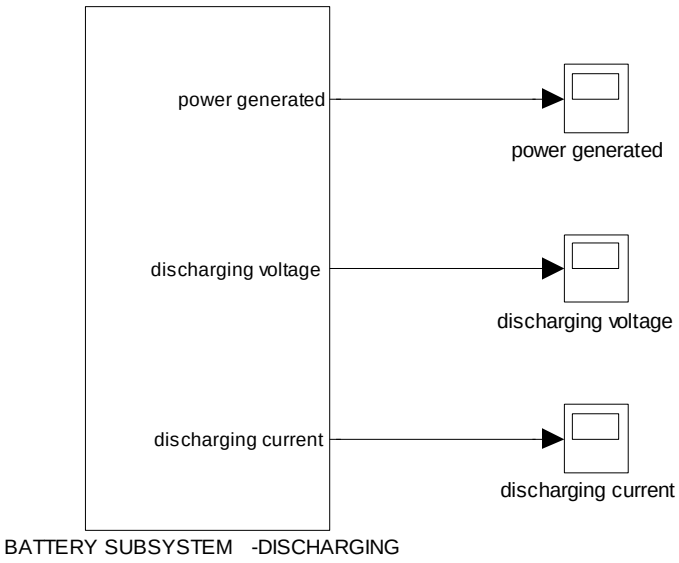

Figure 39: Battery discharging block

The values in Table 6 are considered for the user-defined parameters of the dialog box shown in Fig. 40. A battery with capacity of 200 ampere-hours and state of charge of 85% is assumed for the simulation. Knowing that the battery emf and equivalent load resistance are 100 V and 3.6 Ω, respectively, the discharging current can be assigned by calculating the internal resistance. In this case if a discharging current of 25 A is desired, then the internal resistance would be 0.4 Ω.

Battery emf [volts dc]	100
Internal resistance [ohms]	0.4
Equivalent load resistance [ohms]	3.6
Battery capacity [ampere-hour]	200
Battery state of charge [%]	85

Table 6: Parameters used for simulation of battery discharging model

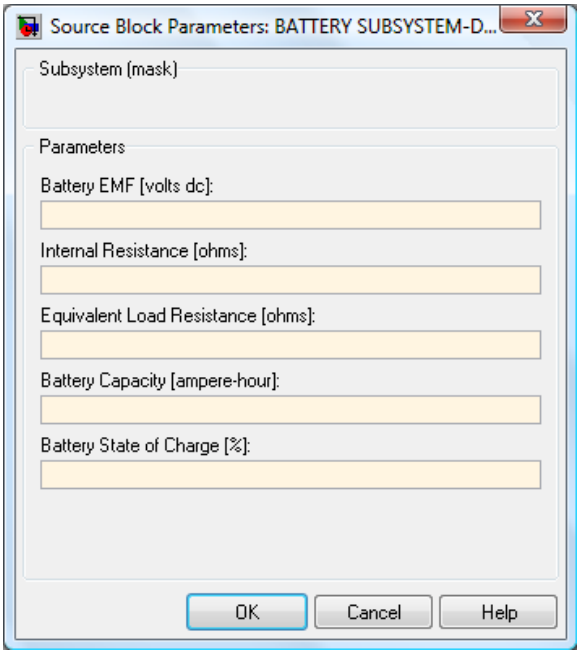

Figure 40: Dialog box for battery discharging model

In Figs. 41-43, simulation results of the battery model during its discharging mode are presented. Here, the simulation is designed to run until the battery is fully discharged, i.e., reaches a state of charge of 0%. Applying (2.19), it is observed that the simulation stops after 6.8 hours, or 24480 seconds.

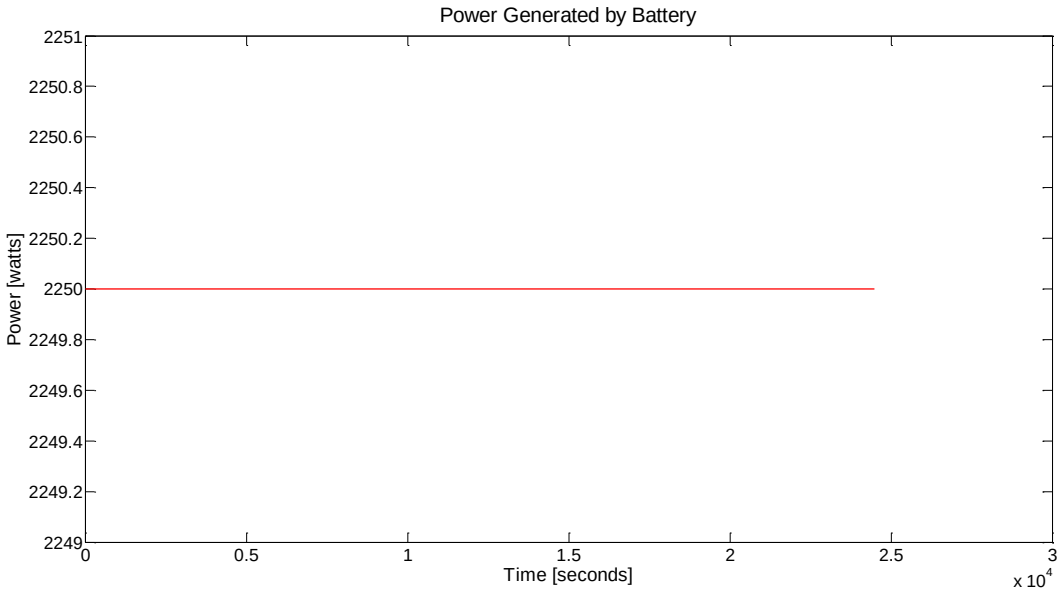

Figure 41: Simulated power generated by battery

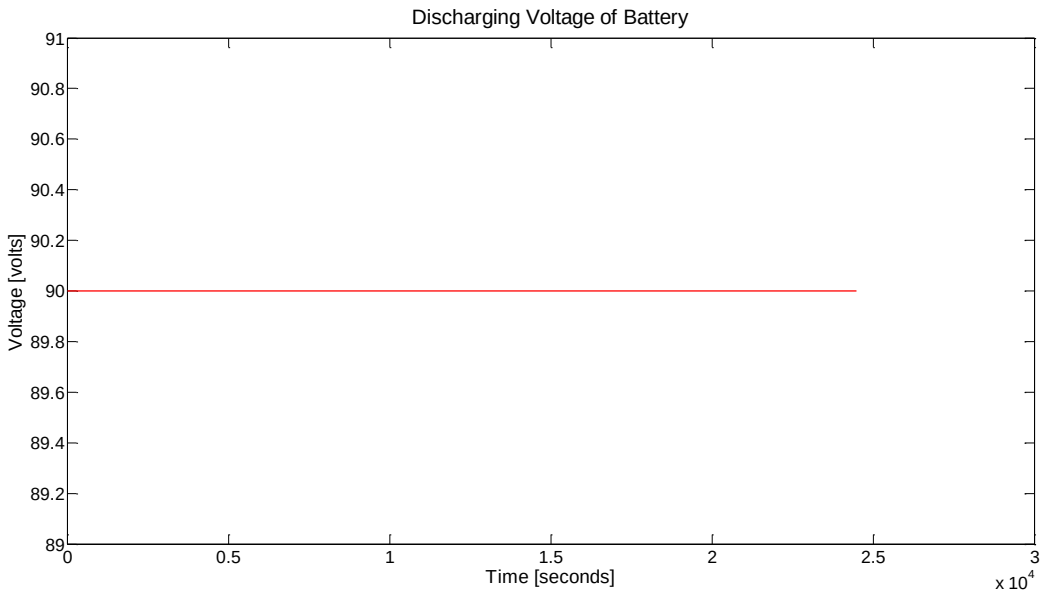

Figure 42: Simulated discharging voltage of battery

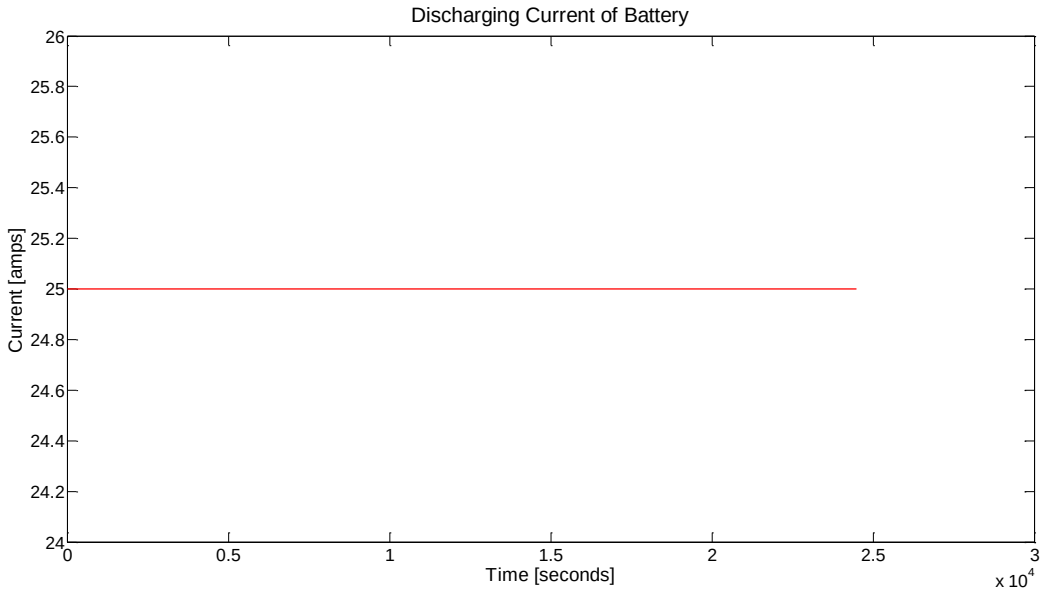

Figure 43: Simulated discharging current of battery

3.5 CONDUCTORS

The simulation results of the ac and dc conductor models are presented.

3.5.1 ac Conductor

Using (2.20) and (2.21), the Simulink block in Fig. 44 is created.

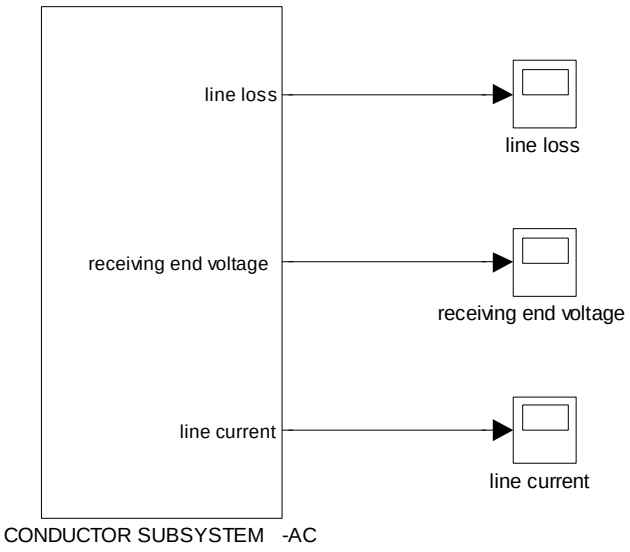

Figure 44: ac conductor block

The values in Table 7 are entered for the parameters requested by the dialog box in Fig. 45. Using the datasheet for aluminum conductor steel reinforced cables [68], and assuming a '4/0' cable of length 1000 ft, the values for R_{line} and L_{line} are estimated in a 12.47 kV system. The simulation results of the ac conductor model are illustrated in Figs. 46-48.

Input voltage [volts ac]	12470
Frequency [hertz]	60
Line resistance [ohms]	0.0822
Line inductance [henries]	0.215
Equivalent load-side resistance [ohms]	300
Equivalent load-side inductance [henries]	0.1

Table 7: Parameters used for simulation of ac conductor model

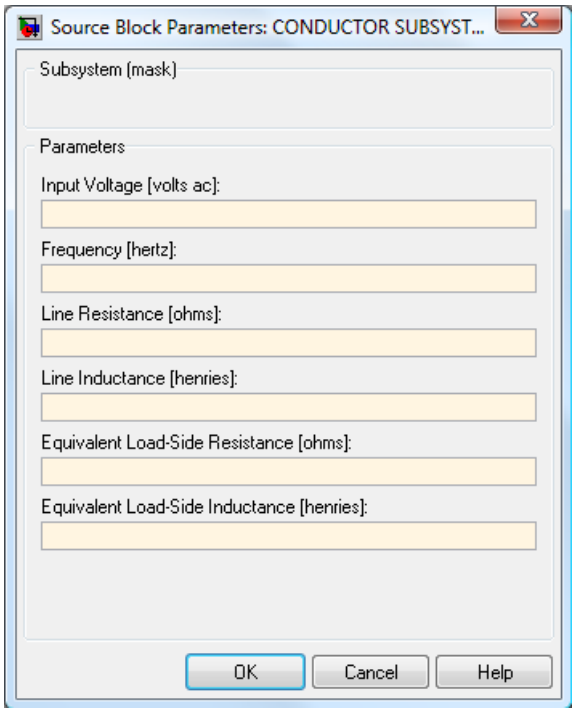

Figure 45: Dialog box for ac conductor model

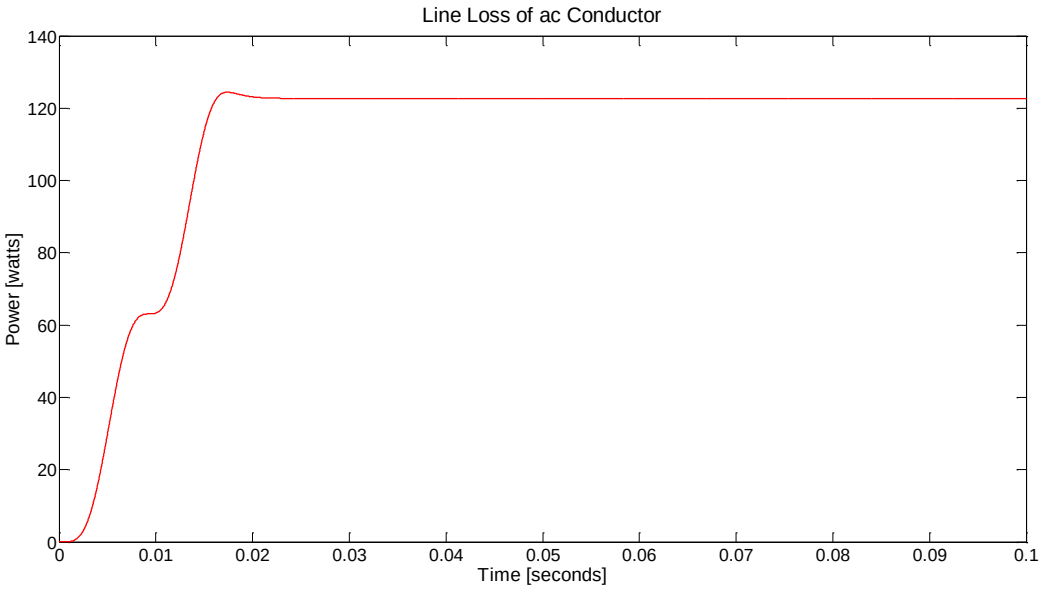

Figure 46: Simulated line loss of ac conductor

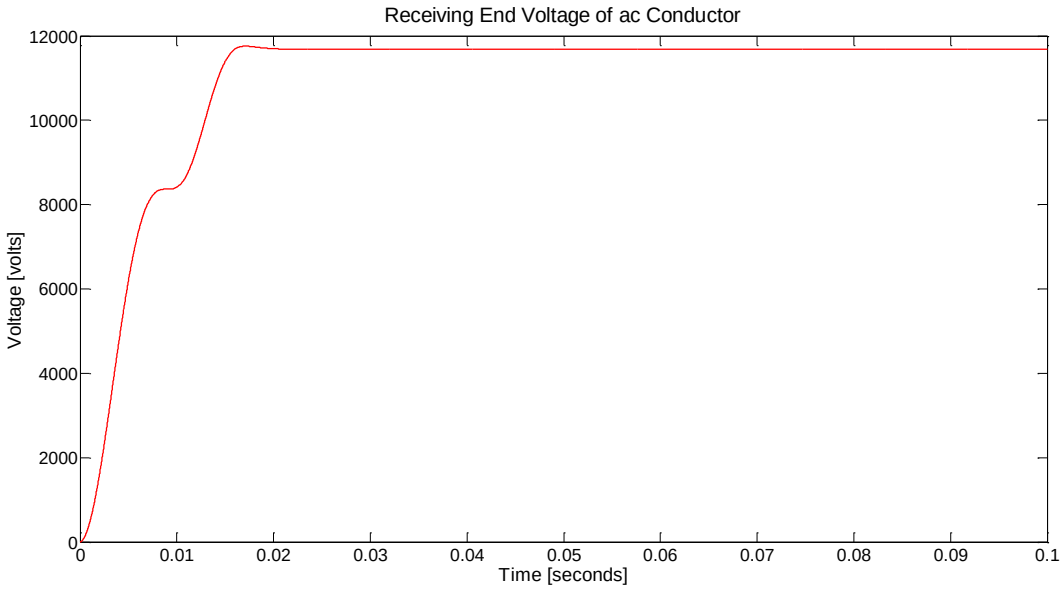

Figure 47: Simulated receiving end voltage of ac conductor

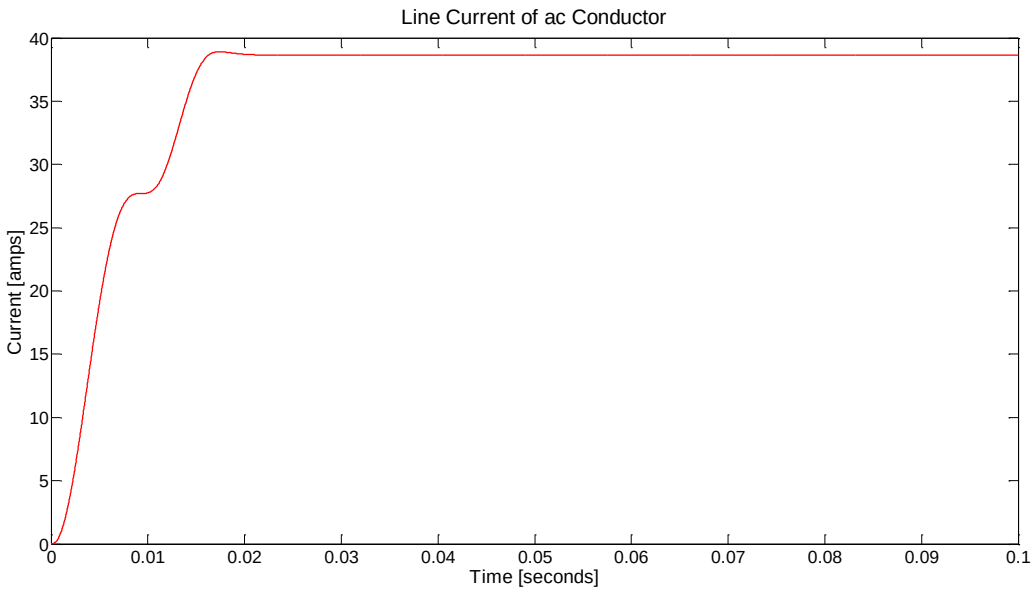

Figure 48: Simulated line current of ac conductor

3.5.2 dc Conductor

The Simulink block in Fig. 49 is created using (2.22) and (2.23).

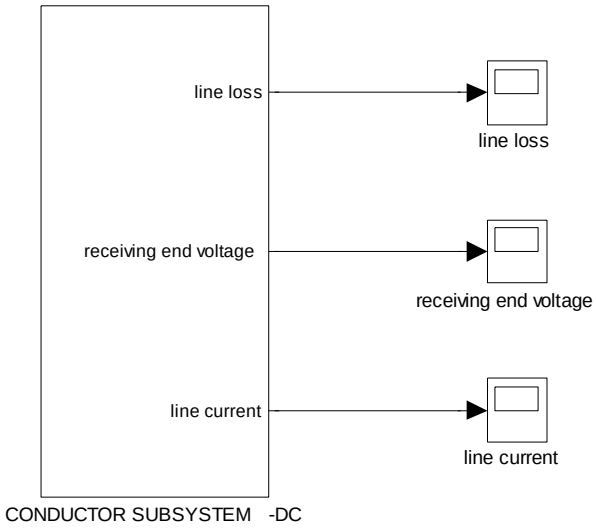

Figure 49: dc conductor block

The values used for the simulation are included in Table 8; these values are entered into the dialog box shown in Fig. 50. Using [68], and assuming a '#4' cable of length 500 ft, the value for R_{line} is estimated in a system with a sending end voltage of 1000 V. The simulation results of the dc conductor model are presented in Figs. 51-53.

Input voltage [volts dc]	1000
Line resistance [ohms]	0.2
Equivalent load-side resistance [ohms]	50

Table 8: Parameters used for simulation of dc conductor model

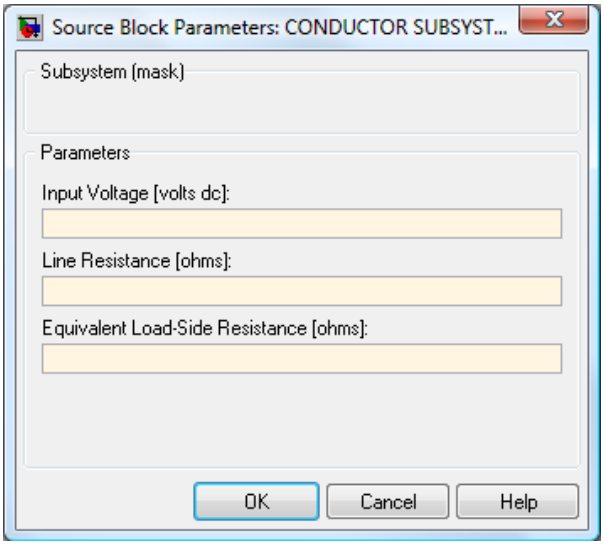

Figure 50: Dialog box for dc conductor model

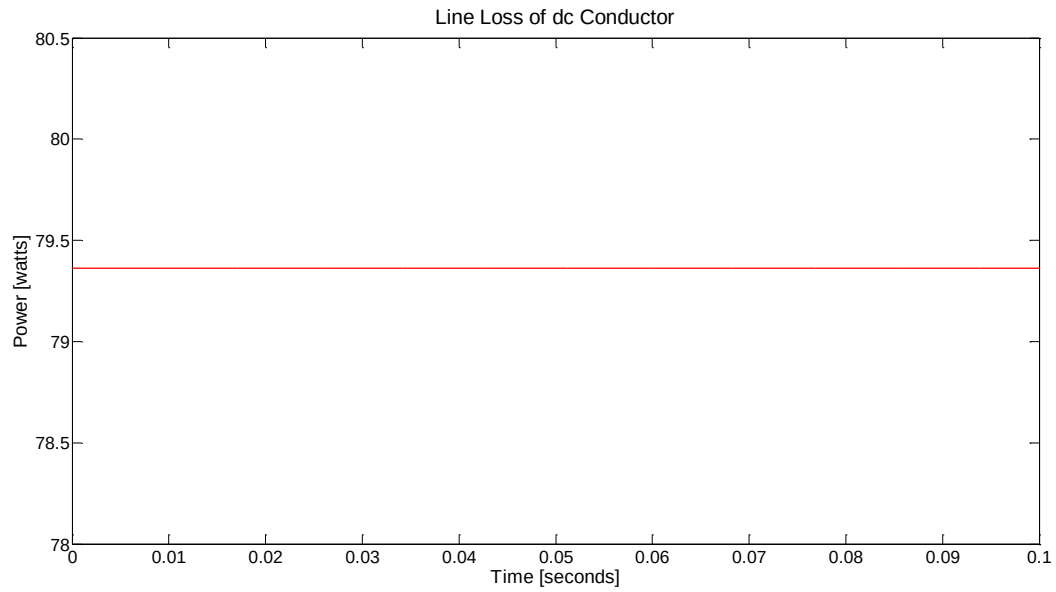

Figure 51: Simulated line loss of dc conductor

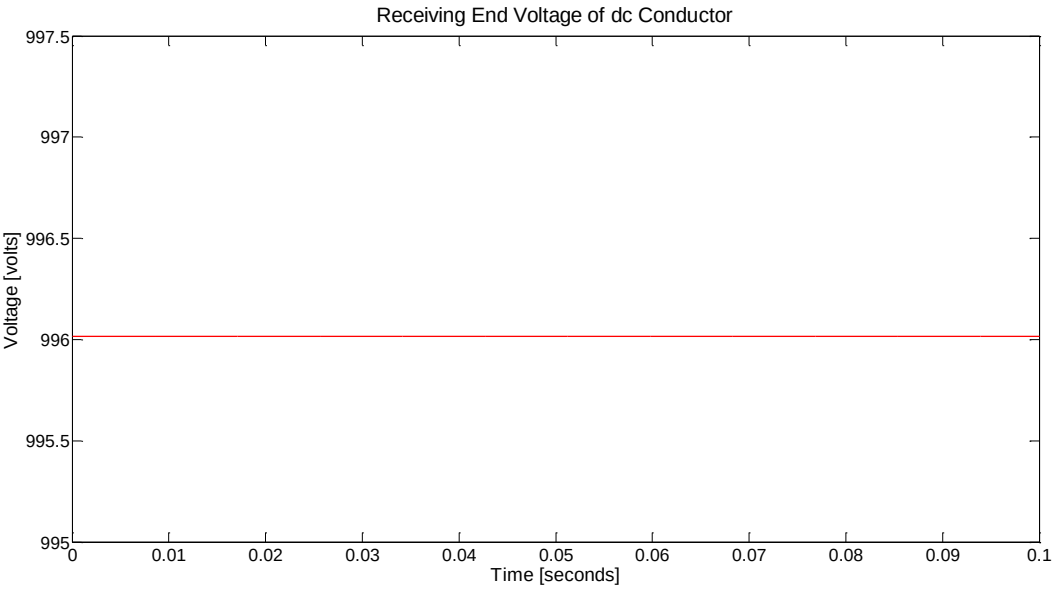

Figure 52: Simulated receiving end voltage of dc conductor

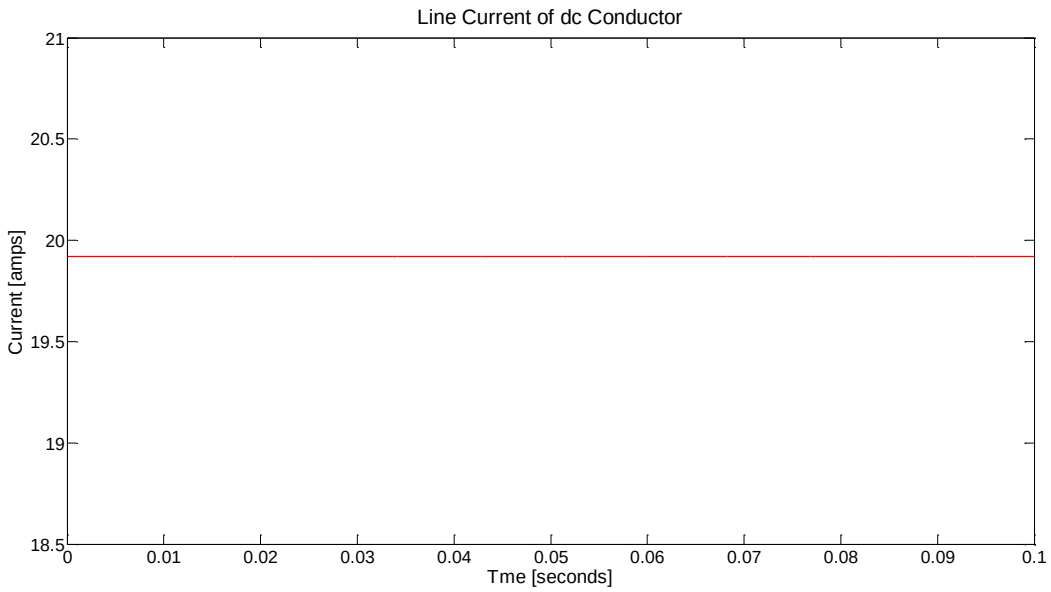

Figure 53: Simulated line current of dc conductor

3.6 PLUG-IN ELECTRIC VEHICLE

Using (2.25)-(2.27), the Simulink block in Fig. 54 is developed. The values in Table 9 are entered into the dialog box shown in Fig. 55.

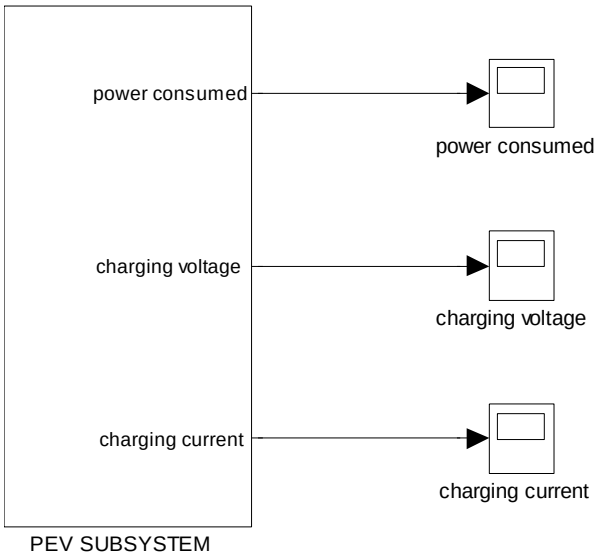

Figure 54: PEV block

Charging voltage [volts ac]	240
Frequency [hertz]	60
Battery resistance [ohms]	30
Battery capacity [ampere-hour]	50
Battery state of charge [%]	10
Rectifier voltage efficiency [%]	92
Rectifier current efficiency [%]	92

Table 9: Parameters used for simulation of PEV model

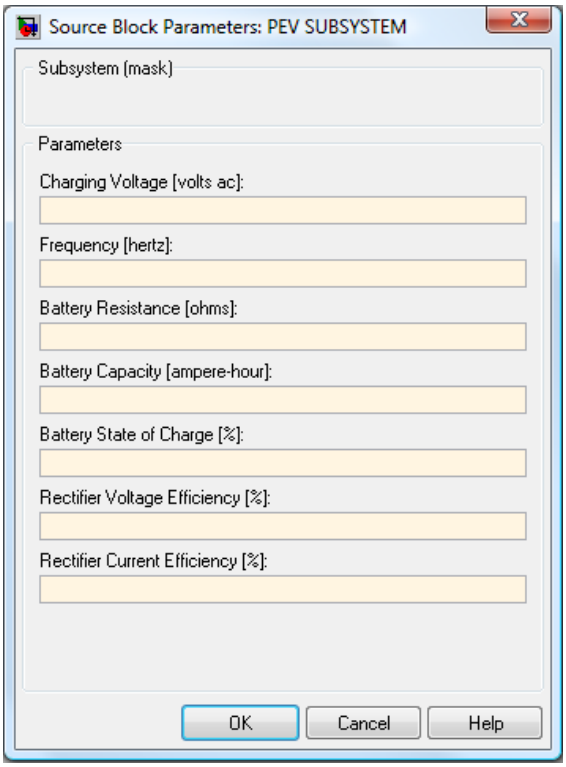

Figure 55: Dialog box for PEV model

An arbitrary value of 92% is chosen for the rectifier's input-output voltage and current efficiency, and it is assumed that the PEV is charged from 240 Vac with 16 A of current provided from the grid, which amounts to 3.84 kW of power consumed from the grid. Applying (2.25) and (2.26), the charging voltage and charging current from the rectifier's perspective are found to be 312.3 Vdc and 10.4 A, respectively. Thus, from the perspective of the rectifier, 3.248 kW of power are consumed by the PEV's battery, which befittingly corresponds to a rectifier efficiency of 85%, i.e., $\eta_v \times \eta_i$. If the PEV battery is assumed to have a capacity of 50 Ah with a state of charge of 10% , then a time of 4.32 hours, or 15,564 seconds, must be elapsed in order to reach full charge, as related by (2.28). The simulation results—power consumed, charging voltage, and charging current—all from the perspective of the grid, are presented in Figs. 56-58.

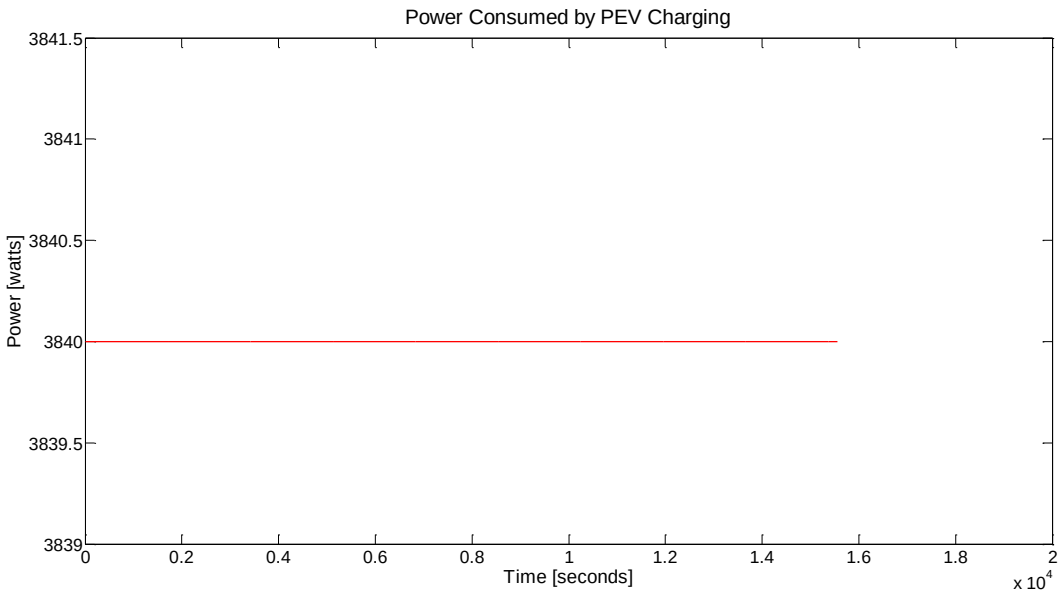

Figure 56: Simulated power consumed by PEV charging

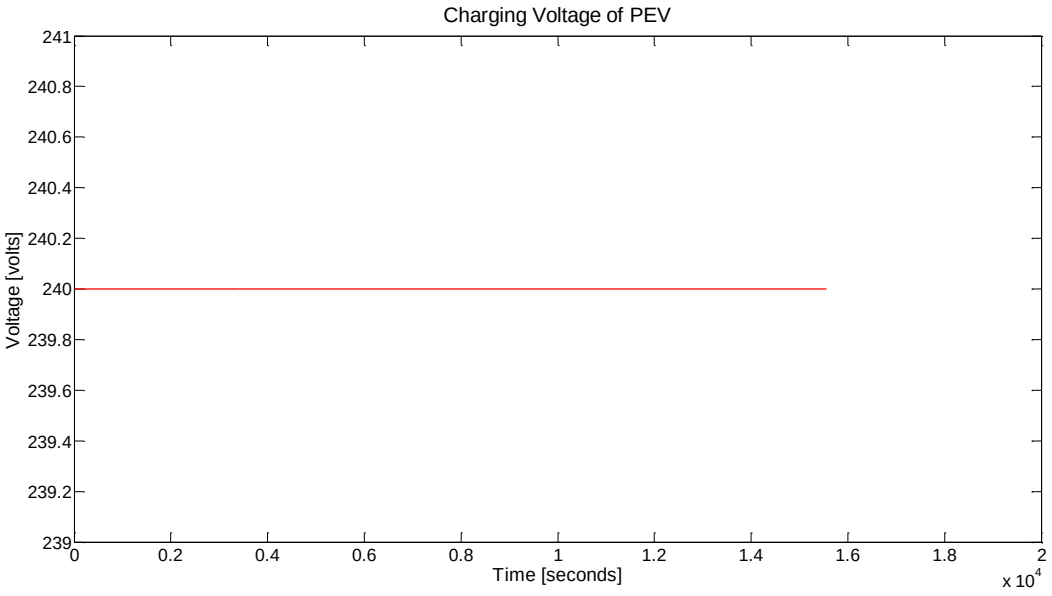

Figure 57: Simulated charging voltage of PEV

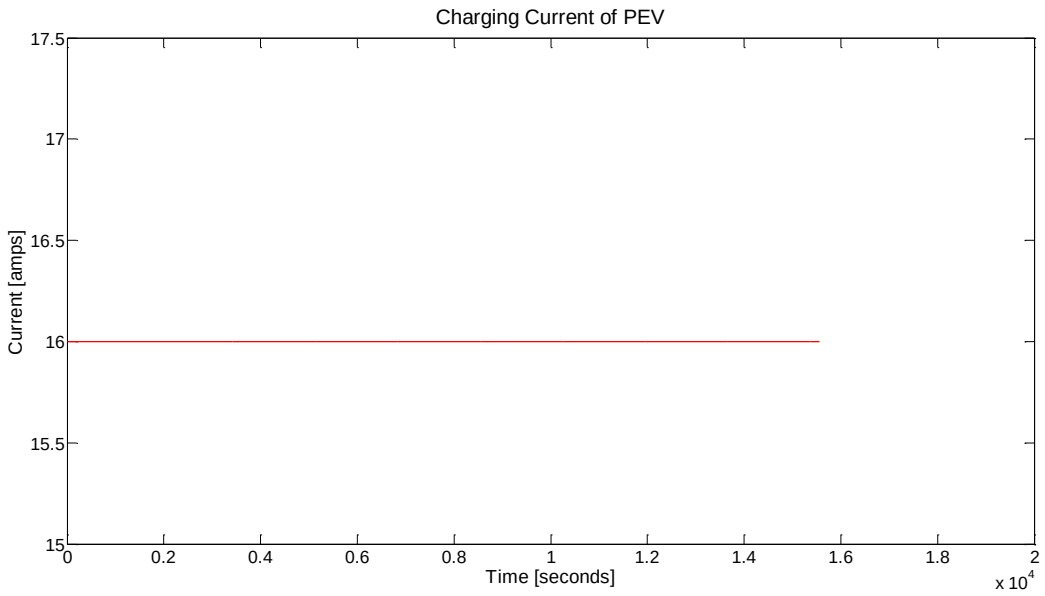

Figure 58: Simulated charging current of PEV

3.7 POWER ELECTRONICS INTERFACE

The simulation results of power electronic devices such as the buck converter, boost converter, rectifier, and inverter are presented.

3.7.1 Buck Converter

The Simulink block for the buck converter, along with its associated dialog box, are shown in Figs. 59 and 60, respectively. The values used for the simulation are specified in Table 10. Assuming an input voltage of 40 V and a switching frequency of 5 kHz, the buck converter model is simulated, and its results are shown in Figs. 61-63. It is observed that the output voltage of the converter converges to 20 V, as indicated by (2.29).

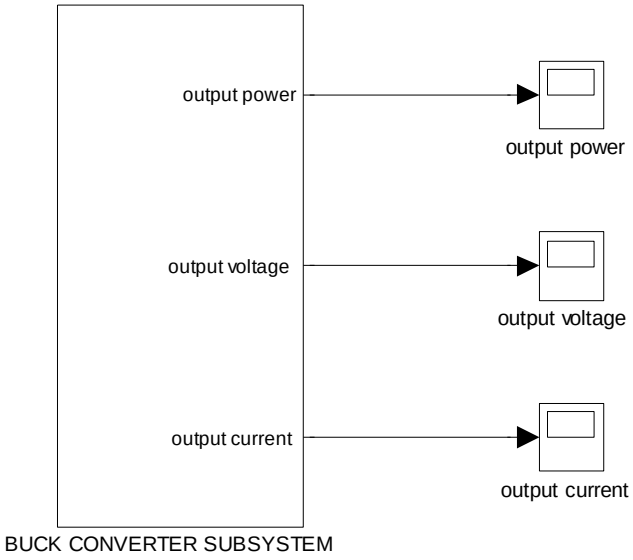

Figure 59: Buck converter block

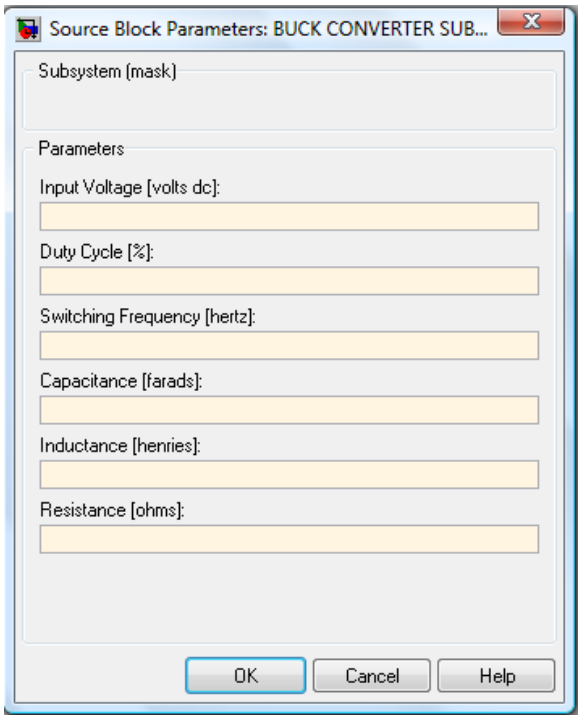

Figure 60: Dialog box for buck converter model

Input voltage [volts dc]	40
Duty cycle [%]	50
Switching frequency [hertz]	5000
Capacitance [farads]	0.001
Inductance [henries]	0.05
Resistance [ohms]	10

Table 10: Parameters used for simulation of buck converter model

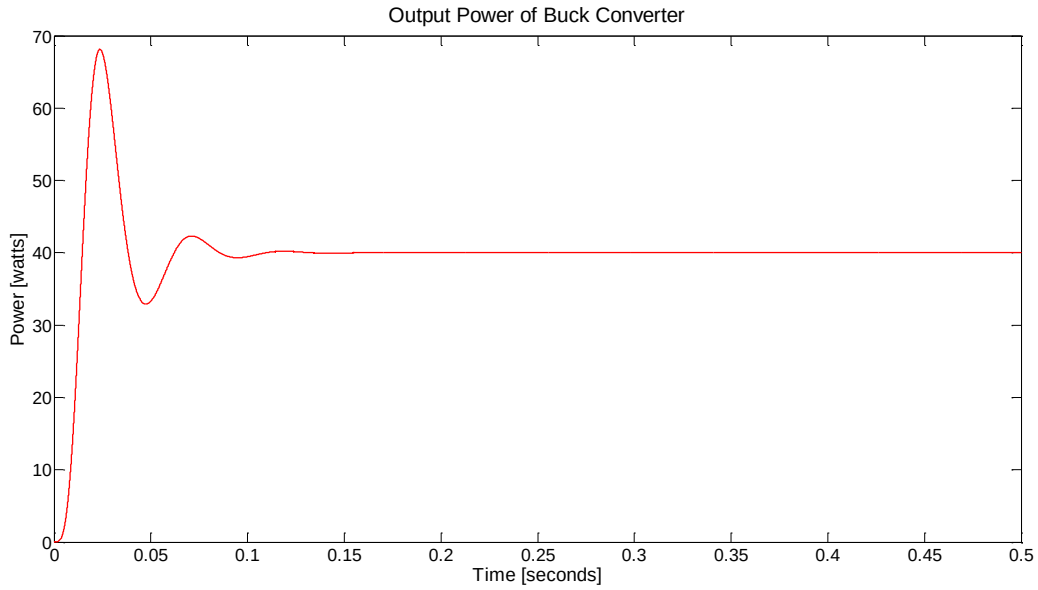

Figure 61: Simulated output power of buck converter

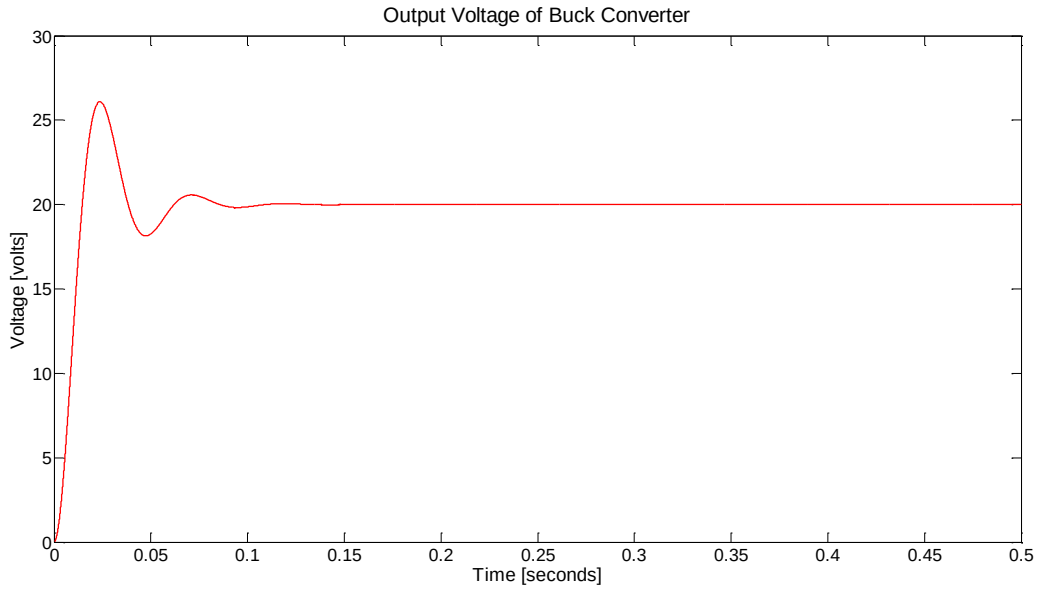

Figure 62: Simulated output voltage of buck converter

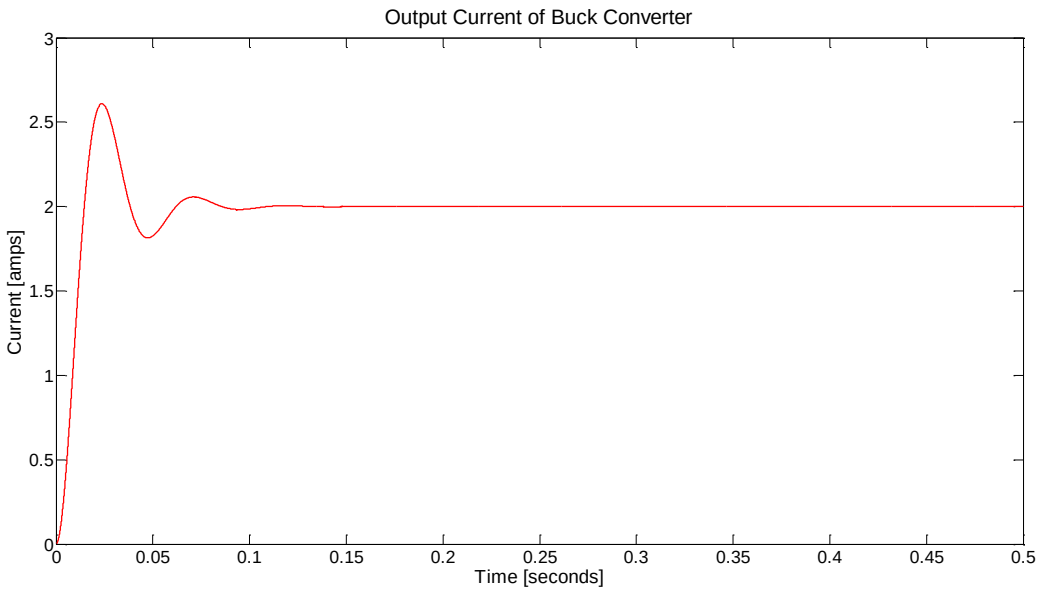

Figure 63: Simulated output current of buck converter

3.7.2 Boost Converter

The boost converter's Simulink block, shown in Fig. 64, is created using (2.33) and (2.34). The values entered into the dialog box of Fig. 65 are tabulated in Table 11. Assuming an input voltage of 30 V and a switching frequency of 5 kHz, the boost converter model is simulated. The results are shown in Figs. 66-68. In agreement with (2.32), the output voltage of the converter converges to 60 V. The boost converter has several applications: it is used in regulated dc power supplies, regenerative braking of dc motors, and maximum power point tracking of PV arrays. Maximum power point tracking is achieved by connecting a boost converter between the PV module and load resistor, and adjusting the duty cycle so that the equivalent load resistance seen by the source is modified to where maximum power is transferred. Additionally, a boost converter can be used to connect a dc bus to any combination of batteries, ultracapacitors, fuel-cells, and PV plants.

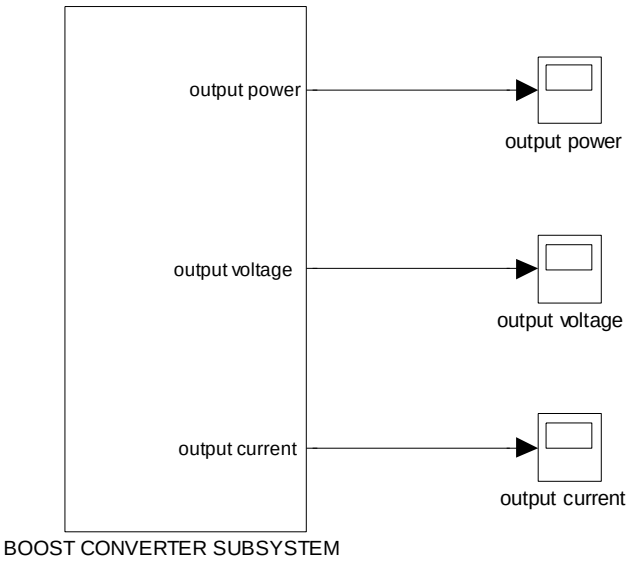

Figure 64: Boost converter block

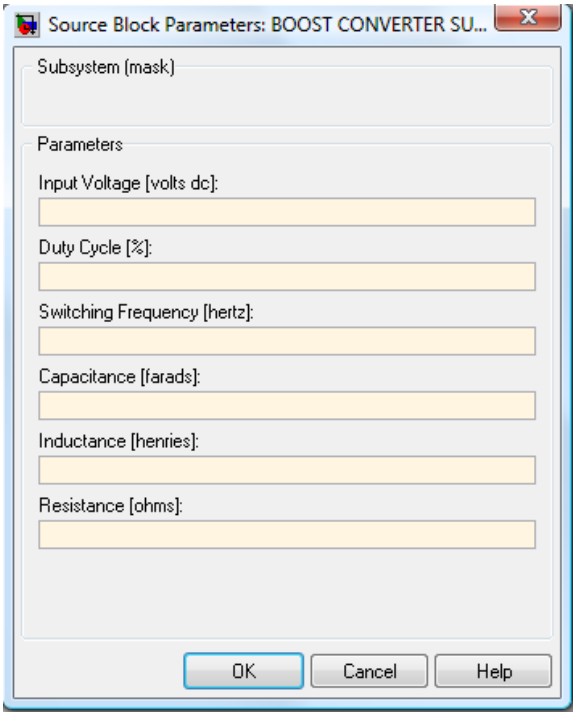

Figure 65: Dialog box for boost converter model

Input voltage [volts ac]	30
Duty cycle [%]	50
Switching frequency [hertz]	5000
Capacitance [farads]	0.001
Inductance [henries]	0.05
Resistance [ohms]	10

Table 11: Parameters used for simulation of boost converter model

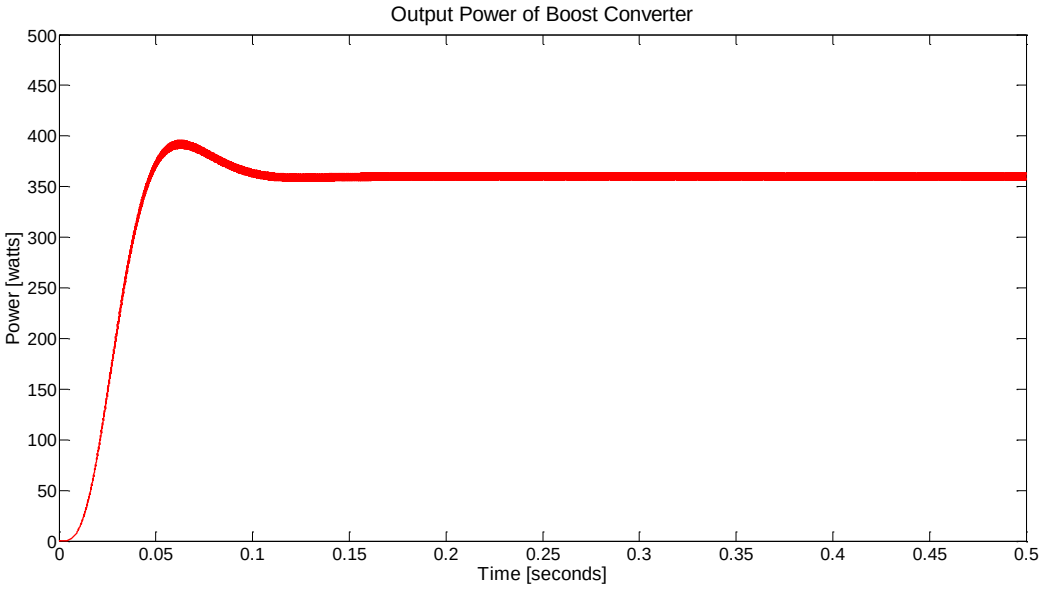

Figure 66: Simulated output power of boost converter

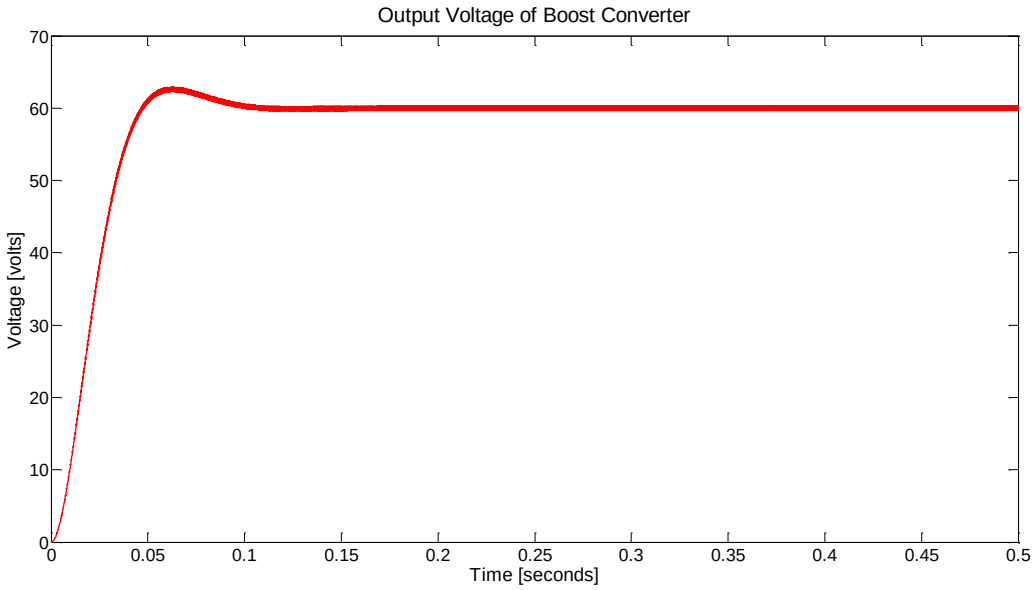

Figure 67: Simulated output voltage of boost converter

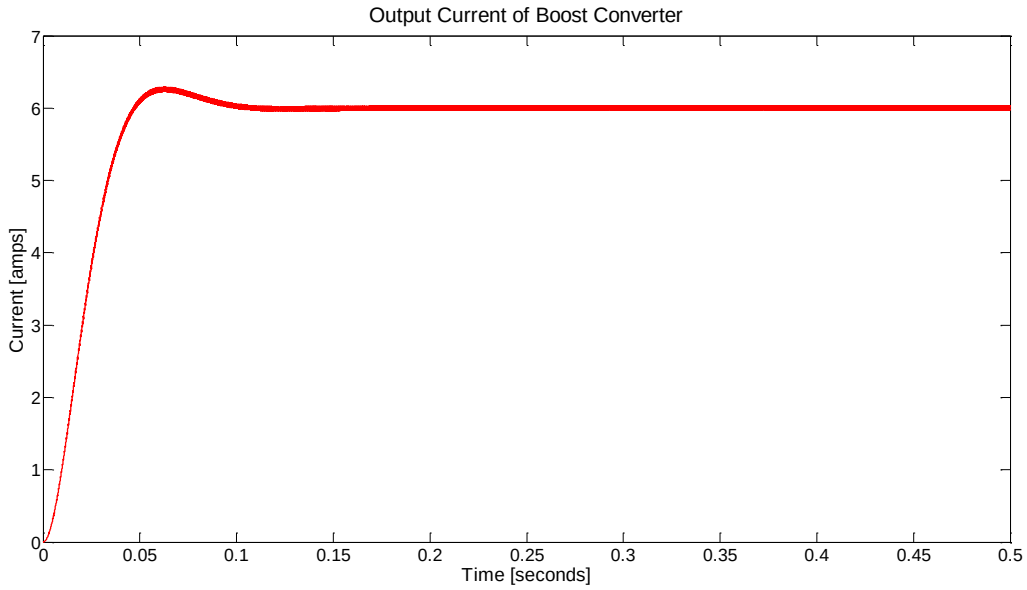

Figure 68: Simulated output current of boost converter

3.7.3 Rectifier

The Simulink block for the rectifier is shown in Fig. 69. The parameters used for the simulation, as well as the associated dialog box are provided in Table 12 and Fig. 70, respectively. The simulation results of the rectifier are shown in Figs. 71-73, where rectification of the input ac signal is evidenced with a unidirectional flow of current. It is observed that the output signal consists of dc along with high-ripple ac components.

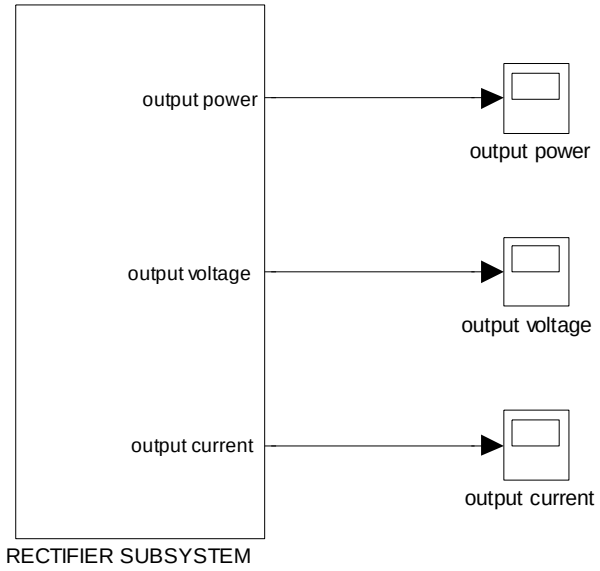

Figure 69: Rectifier block

Input voltage [volts ac]	120
Frequency [hertz]	60
Capacitance [farads]	0.001
Inductance [henries]	0.005
Resistance [ohms]	10

Table 12: Parameters used for simulation of rectifier model

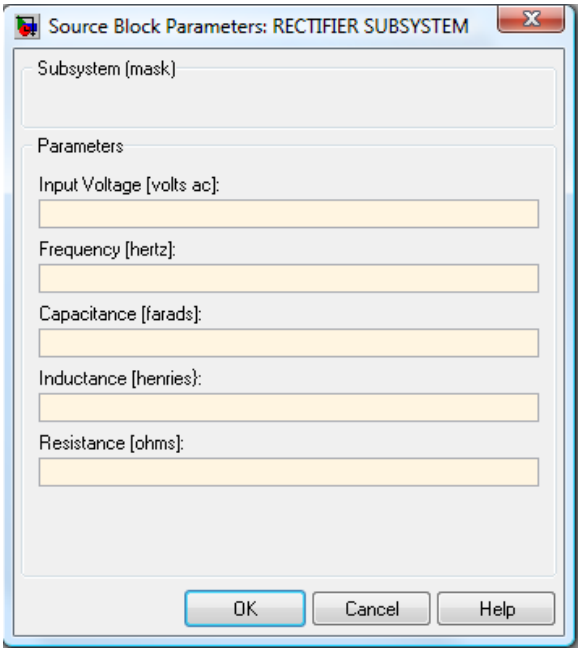

Figure 70: Dialog box for rectifier model

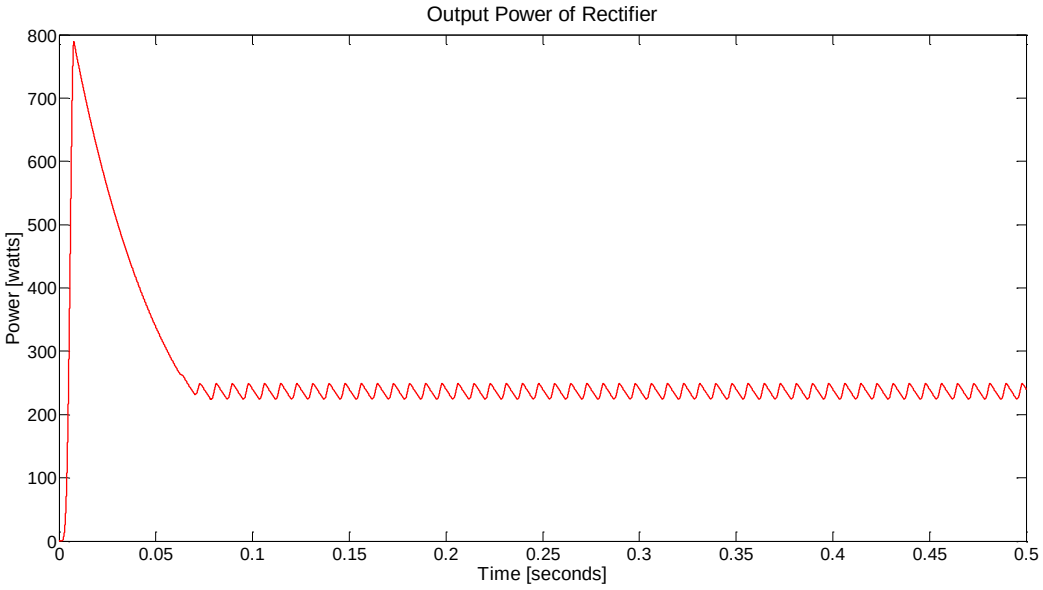

Figure 71: Simulated output power of rectifier

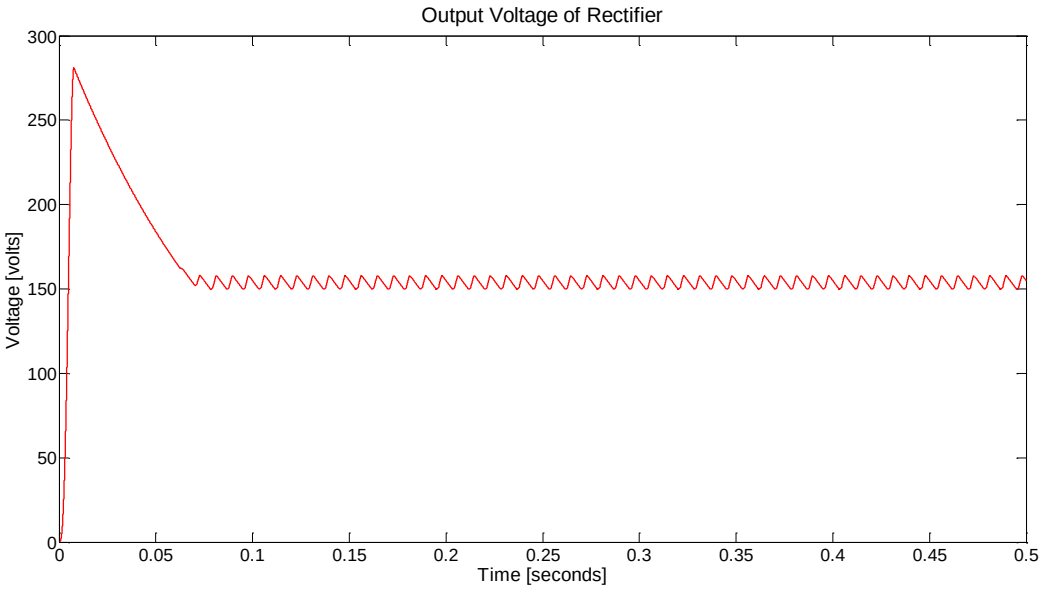

Figure 72: Simulated output voltage of rectifier

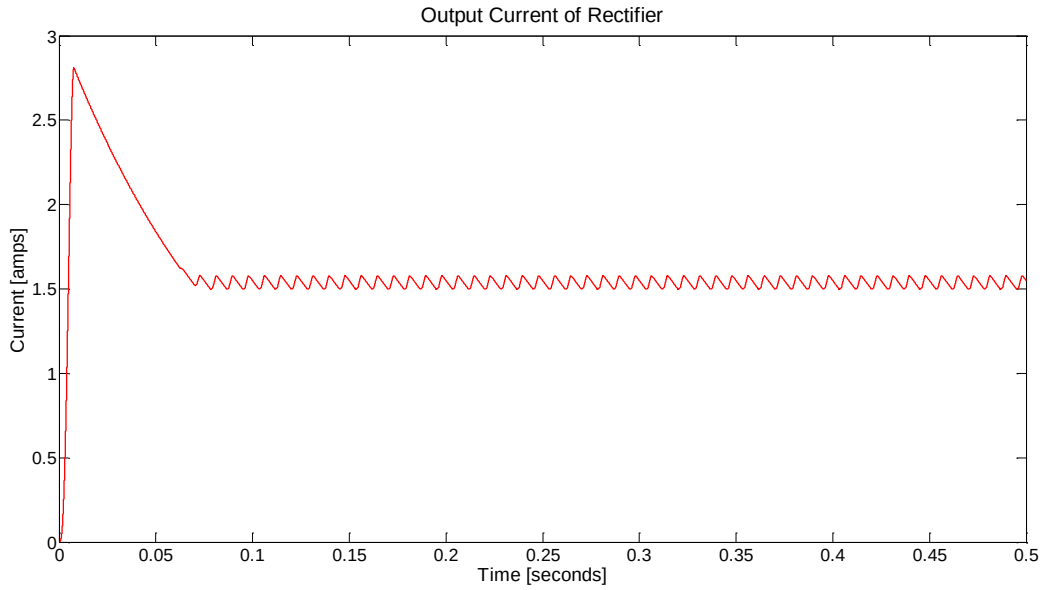

Figure 73: Simulated output current of rectifier

3.7.4 Inverter

Using the equations developed earlier, a Simulink block representing an H-bridge inverter is created and shown in Fig. 74. The values used for the simulation are included in Table 13, and the dialog box requesting these parameters is shown in Fig. 75.

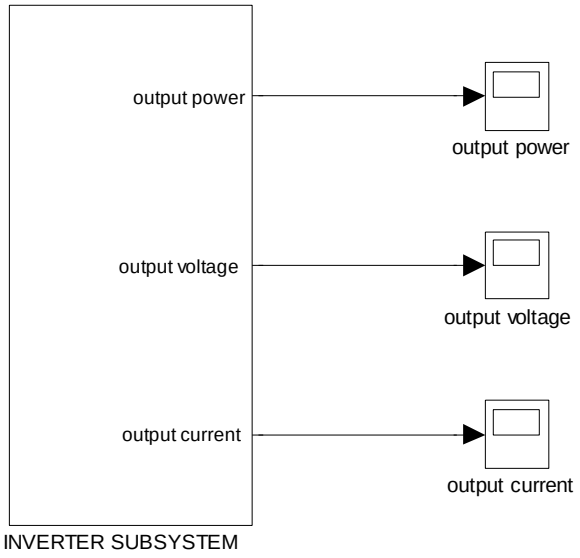

Figure 74: Inverter block

Input voltage [volts dc]	100
Sine wave frequency [hertz]	60
Triangle wave frequency [hertz]	123,000
Modulation amplitude m_a	0.95
Load resistance [ohms]	1.5
Filter capacitance [farads]	3.79×10^{-9}
Filter inductance [henries]	0.442×10^{-3}

Table 13: Parameters used for simulation of inverter model

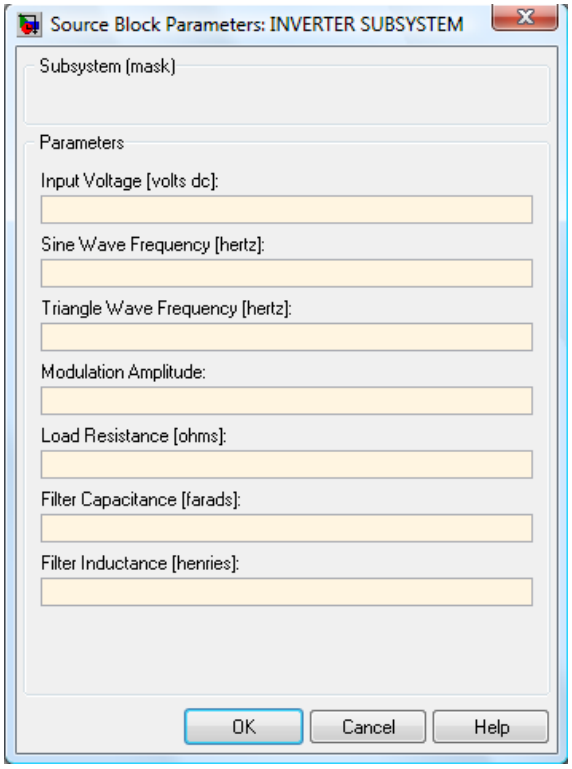

Figure 75: Dialog box for inverter model

This particular inverter, which is designed for a 3 kW application, has a switching frequency of 123 kHz and modulation amplitude of 0.95. The filter, whose design and derivation is not pertinent to the scope of this thesis, allows the fundamental component to pass and limits the passage of harmonics, thereby minimizing distortion. The presence of harmonics is evident in the load voltage waveform $V_a - V_b$ depicted in Fig. 76. Once the filter is applied, the fundamental component of the output voltage becomes apparent, as shown in Fig. 77. Therefore, the inverter successfully produces an ac output from a dc input via appropriate PWM switching. Other simulation results involving the output power, output voltage, and output current are provided in Figs. 78-80, respectively.

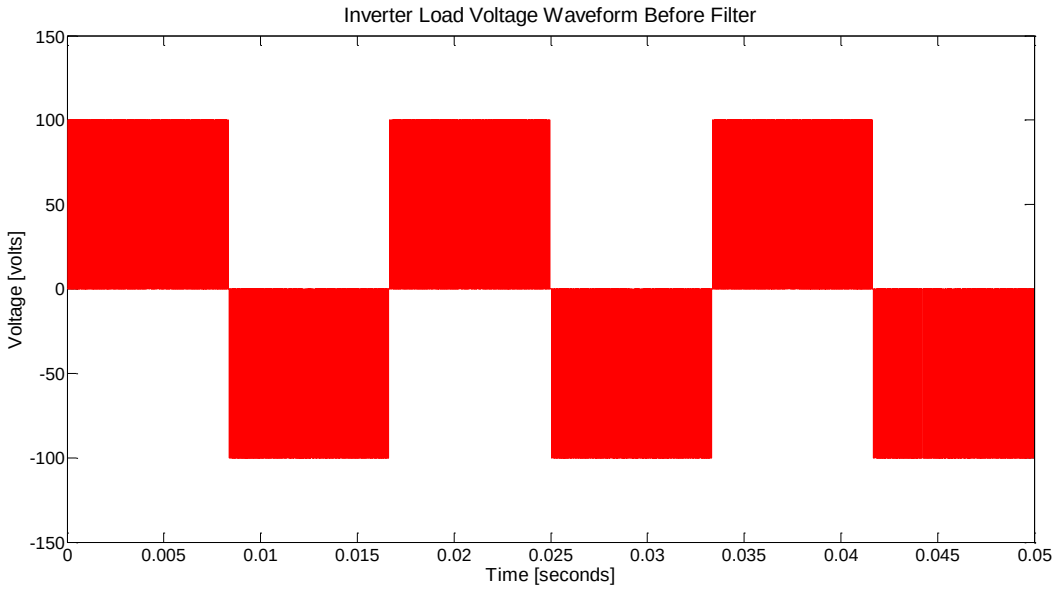

Figure 76: Simulated load voltage waveform before filter

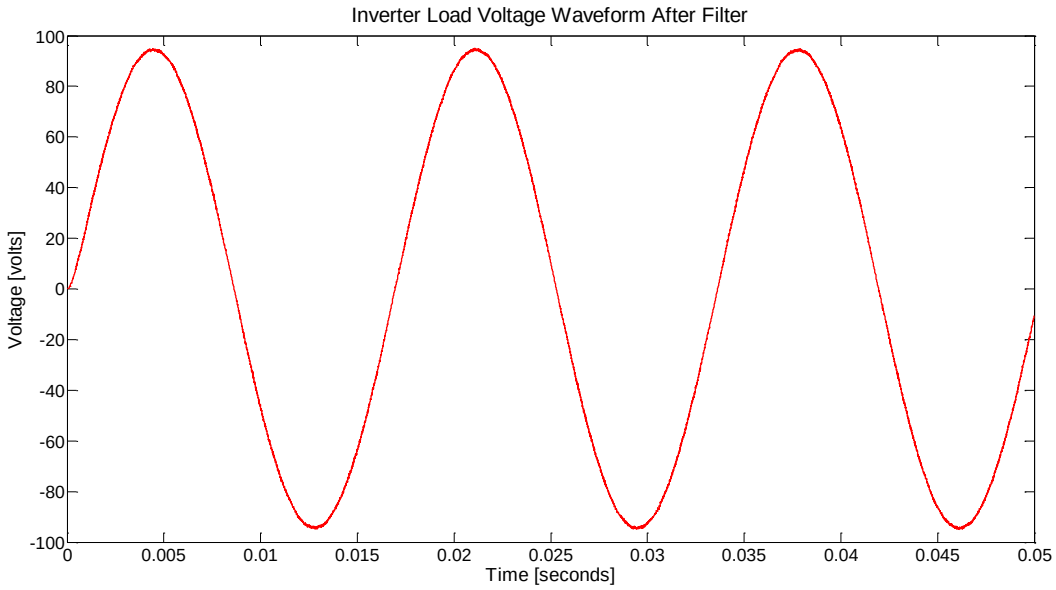

Figure 77: Simulated load voltage waveform after filter

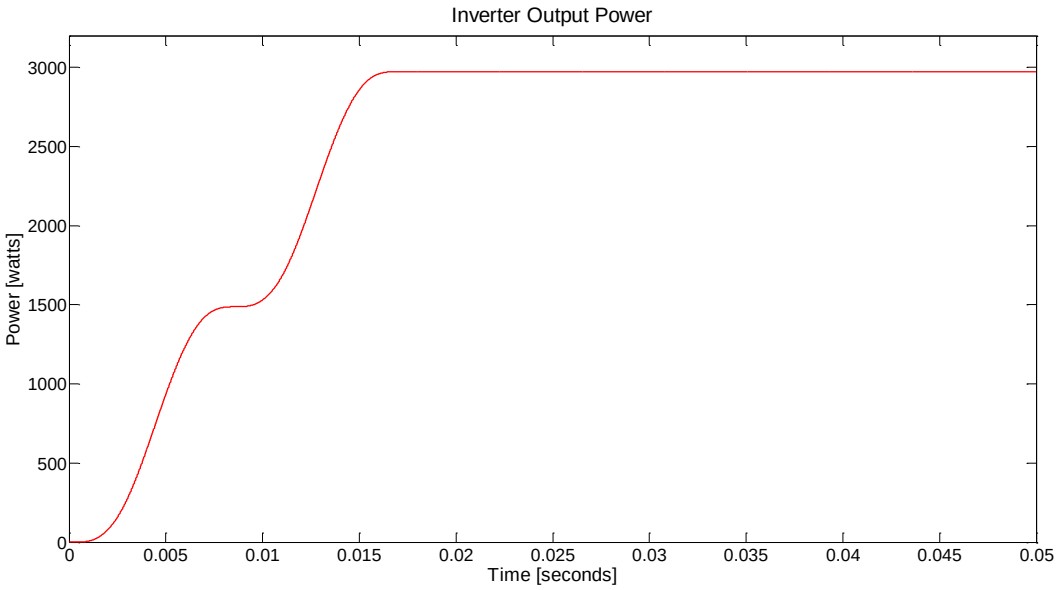

Figure 78: Simulated output power of inverter

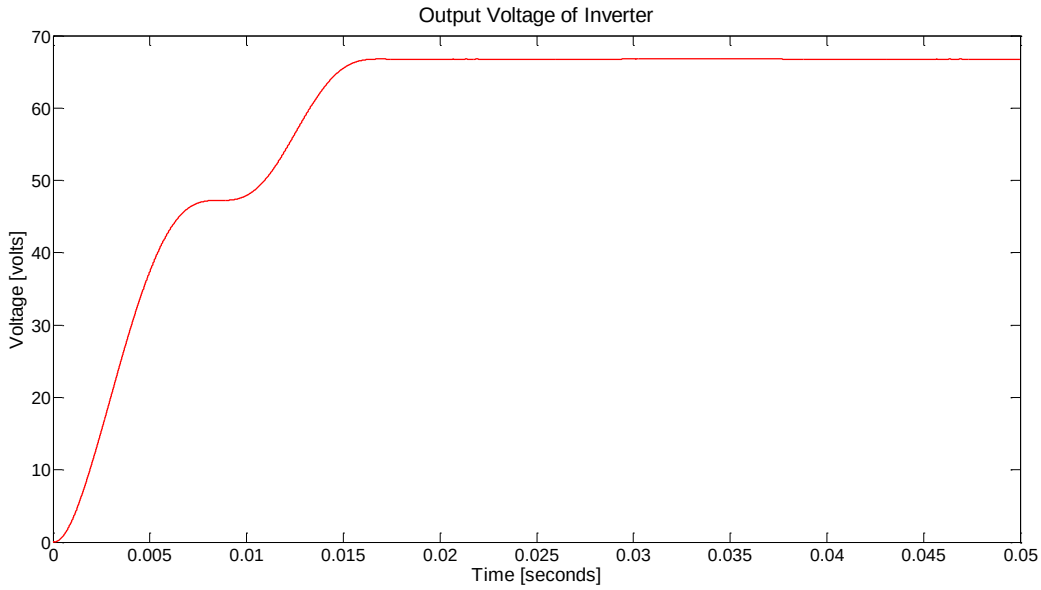

Figure 79: Simulated output voltage of inverter

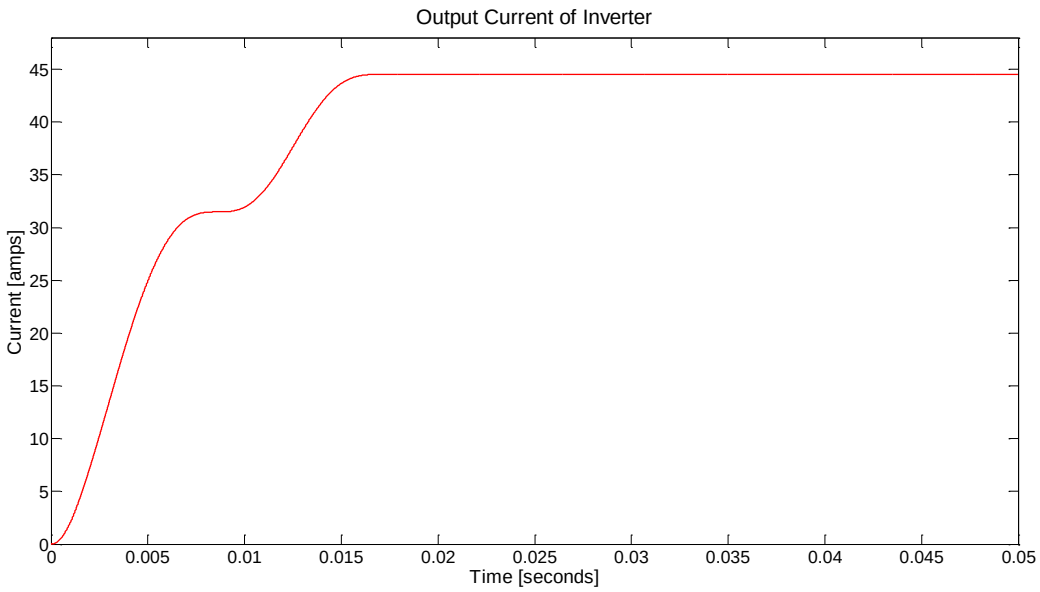

Figure 80: Simulated output current of inverter

Chapter 4: Conclusion

The expected transition from the passive unidirectional power flow of a central source to distributed end-users, to the active two-way power flow of distributed generation, represents a revolution with respect to the traditional concept of a power system. Furthermore, since power electronic apparatuses and electrical drives are becoming more widely used for energy conversion, the ability to maintain prefixed levels of power quality will become a reason for concern. Also, in addition to the increased requirements and needs of end-users, widespread adoption of distributed generation will engender high levels of complexity in the management and operation of the grid. The stability of networks must also be studied in the presence of variable and renewable energy sources. All these reasons contribute to the motivation for developing a framework to model the impacts of smart grids, and in so doing, accelerating the grid transformation process.

The modeling and simulation of distribution system components pertinent to a smart grid was presented in this thesis. The components considered in this work included PV arrays, the electric grid, an air conditioning load, energy storage, conductors, PEVs, and power electronic interfaces. The methodology involved deriving the equations of the components and creating modules in Simulink that mask the relevant components' equations. The ultimate goal is to connect the individual modules together via a voltage interface to perform various analyses, such as the evaluation of harmonics; or general studies involving capacity, runtime, and the interdependency between generation and consumption.

Future work will incorporate stochastic processes in the modeling, especially with regard to PV generation, since optimal sizing of PV arrays and energy storage depends on randomly behaving parameters. Other factors such as cloud coverage of PV arrays may need to be considered, in order to increase the accuracy of the models and to allow for better predictions of variability. Nonlinear loads will also be modeled to investigate the effects of harmonics, and more accurate battery models are to be developed instead of making simplifying assumptions.

Bibliography

[1] U.S. Department of Homeland Security, Science and Technology Directorate. *National Power Grid Simulation Capability: Needs and Issues*. Argonne, Illinois, December 2008.

[2] Kersting, W.H. *Distribution System Modeling and Analysis*. CRC Press, 2002.

[3] Center for American Progress. *A National Clean-Energy Smart Grid 101*. February 23, 2009.

[4] National Energy Technology Laboratory. *A Vision for the Modern Grid*. March 2007.

[5] Keyhani, Ali, Mohammad N. Marwali, and Min Dai. *Integration of Green and Renewable Energy in Electric Power Systems*. John Wiley, 2010.

[6] M.E. Ropp and S. Gonzalez, "Development of a MATLAB/Simulink Model of a Single-Phase Grid-Connected Photovoltaic System," *IEEE Transactions on Energy Conversion*, vol.24, no.1, pp.195-202, March 2009.

[7] M.G. Villalva, J.R. Gazoli, and E.R. Filho, "Comprehensive Approach to Modeling and Simulation of Photovoltaic Arrays," *IEEE Transactions on Power Electronics* , vol.24, no.5, pp.1198-1208, May 2009.

[8] H. S. Rauschenbach, *Solar Cell Array Design Handbook*. New York: Van Nostrand Reinhold, 1980.

[9] J. A. Gow and C. D. Manning, “Development of a photovoltaic array model for use in power-electronics simulation studies,” *IEE Proc. Elect. Power Appl.,* vol. 146, no. 2, pp. 193-200, 1999.

[10] J. A. Gow and C. D. Manning, “Development of a model for photovoltaic arrays suitable for use in simulation studies of solar energy conversion systems,” in *Proc. 6th Int. Conf. Power Electron. Variable Speed Drives,* 1996, pp. 69-74.

[11] N. Pongratananukul and T. Kasparis, “Tool for automated simulation of solar arrays using general-purpose simulators,” in *Proc. IEEE Workshop Comput. Power Electron.,* 2004, pp. 10-14.

[12] S. Chowdhury, G. A. Taylor, S. P. Chowdhury, A. K. Saha, and Y. H. Song, “Modelling, simulation and performance analysis of a PV array in an embedded environment,” in *Proc. 42nd Int. Univ. Power Eng. Conf. (UPEC),* 2007, pp. 781-785.

[13] J. Hyvarinen and J. Karila, "New analysis method for crystalline silicon cells," in *Proc. 3rd World Conf. Photovoltaic Energy Convers.*, 2003, vol. 2, pp. 1521-1524.

[14] K. Nishioka, N. Sakitani, Y. Uraoka, and T. Fuyuki, "Analysis of multicrystalline silicon solar cells by modified 3-diode equivalent circuit model taking leakage current through periphery into consideration," *Solar Energy Mater. Solar Cells*, vol. 91, no. 13, pp. 1222-1227, 2007.

[15] K. Khouzam, C. Khoon Ly, C. Koh, and P. Y. Ng, "Simulation and realtime modelling of space photovoltaic systems," in *Proc. IEEE 1st World Conf.Photovoltaic Energy Convers.,Conf.Record 24th IEEE Photovoltaic Spec. Conf.*, 1994, vol. 2, pp. 2038–2041.

[16] M. C. Glass, "Improved solar array power point model with SPICE realization," in *Proc. 31st Intersoc. Energy Convers. Eng. Conf. (IECEC)*, Aug. 1996, vol. 1, pp. 286–291.

[17] I. H. Altas and A. M. Sharaf, "A photovoltaic array simulation model for matlab–simulink GUI environment," in *Proc. Int. Conf. Clean Elect. Power (ICCEP)*, 2007, pp. 341–345.

[18] E. Matagne, R. Chenni, and R. El Bachtiri, "A photovoltaic cell model based on nominal data only," in *Proc. Int. Conf. Power Eng., Energy Elect. Drives, POWERENG*, 2007, pp. 562–565.

[19] Y. T. Tan, D. S. Kirschen, and N. Jenkins, "A model of PV generation suitable for stability analysis," *IEEE Trans. Energy Convers.*, vol. 19, no. 4, pp. 748–755, Dec. 2004.

[20] A. Kajihara and A. T. Harakawa, "Model of photovoltaic cell circuits under partial shading," in *Proc. IEEE Int. Conf. Ind. Technol. (ICIT)*, 2005, pp. 866–870.

[21] N. D. Benavides and P. L. Chapman, "Modeling the effect of voltage ripple on the power output of photovoltaic modules," *IEEE Trans. Ind. Electron.*, vol. 55, no. 7, pp. 2638–2643, Jul. 2008.

[22] W. Xiao, W. G. Dunford, and A. Capel, "A novel modeling method for photovoltaic cells," in *Proc. IEEE 35th Annu. Power Electron. Spec. Conf. (PESC)*, 2004, vol. 3, pp. 1950-1956.

[23] E. Koutroulis, K. Kalaitzakis, and V. Tzitzilonis. (2008). Development of a FPGA-based system for real time simulation of photovoltaic modules, *Microelectron. J.* [Online].

[24] E. Koutroulis, K. Kalaitzakis, and V. Tzitzilonis. (2008). Development of a FPGA-based system for real-time simulation of photovoltaic modules, *Microelectron. J.* [Online].

[25] G. Walker, "Evaluating MPPT converter topologies using a matlab PV model," *J. Elect. Electron. Eng., Australia*, vol. 21, no. 1, pp. 45–55, 2001.

[26] M. Veerachary, "PSIM circuit-oriented simulator model for the nonlinear photovoltaic sources," *IEEE Trans. Aerosp. Electron. Syst.*, vol. 42, no. 2, pp. 735–740, Apr. 2006.

[27] A. N. Celik and N. Acikgoz, "Modelling and experimental verification of the operating current of mono-crystalline photovoltaic modules using four- and five-parameter models," *Appl. Energy*, vol. 84, no. 1, pp. 1–15, Jan. 2007.

[28] Y.-C. Kuo, T.-J. Liang, and J.-F. Chen, "Novel maximum-power-point tracking controller for photovoltaic energy conversion system," *IEEE Trans. Ind. Electron.*, vol. 48, no. 3, pp. 594–601, Jun. 2001.

[29] M. T. Elhagry, A. A. T. Elkousy, M. B. Saleh, T. F. Elshatter, and E. M. Abou-Elzahab, "Fuzzy modeling of photovoltaic panel equivalent circuit," in *Proc. 40th Midwest Symp. Circuits Syst.*, Aug. 1997, vol. 1, pp. 60–63.

[30] S. Liu and R. A. Dougal, "Dynamic multiphysics model for solar array," *IEEE Trans. Energy Convers.*, vol. 17, no. 2, pp. 285–294, Jun. 2002.

[31] Y. Yusof, S. H. Sayuti, M. Abdul Latif, and M. Z. C. Wanik, "Modeling and simulation of maximum power point tracker for photovoltaic system," in *Proc. Nat. Power Energy Conf. (PEC)*, 2004, pp. 88–93.

[32] D. Sera, R. Teodorescu, and P. Rodriguez, "PV panel model based on datasheet values," in *Proc. IEEE Int. Symp. Ind. Electron. (ISIE)*, 2007, pp. 2392–2396.

[33] M. A. Vitorino, L. V. Hartmann, A. M. N. Lima, and M. B. R. Correa, "Using the model of the solar cell for determining the maximum power point of photovoltaic systems," in *Proc. Eur. Conf. Power Electron. Appl.*, 2007, pp. 1–10.

[34] D. Dondi, D. Brunelli, L. Benini, P. Pavan, A. Bertacchini, and L. Larcher, "Photovoltaic cell modeling for solar energy powered sensor networks," in *Proc. 2nd Int. Workshop Adv. Sens. Interface (IWASI)*, 2007, pp. 1–6.

[35] H. Patel and V. Agarwal, "MATLAB-based modeling to study the effects of partial shading on PV array characteristics," *IEEE Trans. Energy Convers.*, vol. 23, no. 1, pp. 302–310, Mar. 2008.

[36] W.Yi-Bo,W. Chun-Sheng, L. Hua, and X.Hong-Hua, "Steady-state model and power flow analysis of grid-connected photovoltaic power system," in *Proc. IEEE Int. Conf. Ind. Technol. (ICIT'08)*, pp. 1–6.

[37] W. De Soto, S.A. Klein, and W. A. Beckman, "Improvement and validation of a model for photovoltaic array performance," *Solar Energy*, vol. 80, no. 1, pp. 78–88, Jan. 2006.

[38] Q. Kou, S. A. Klein, and W. A. Beckman, “A method for estimating the long-term performance of direct-coupled PV pumping systems,” *Solar Energy*, vol. 64, no. 1–3, pp. 33–40, Sep. 1998.

[39] A. Driesse, S. Harrison, and P. Jain, “Evaluating the effectiveness of maximum power point tracking methods in photovoltaic power systems using array performance models,” in *Proc. IEEE Power Electron. Spec. Conf. (PESC)*, 2007, pp. 145–151.

[40] R. A. Messenger and J.Ventre, *Photovoltaic Systems Engineering*. Boca Raton, FL: CRC Press, 2004.

[41] F. Nakanishi, T. Ikegami, K. Ebihara, S. Kuriyama, and Y. Shiota, “Modeling and operation of a 10 kW photovoltaic power generator using equivalent electric circuit method,” in *Proc.Conf.Record 28th IEEE Photovoltaic Spec. Conf.*, Sep. 2000, pp. 1703–1706.

[42] J. Crispim, M. Carreira, and R. Castro, “Validation of photovoltaic electrical models against manufacturers data and experimental results,” in *Proc. Int. Conf. Power Eng., Energy Elect. Drives, POWERENG*, 2007, pp. 556–561.

[43] K. H. Hussein, I. Muta, T. Hoshino, and M. Osakada, “Maximum photovoltaic power tracking: An algorithm for rapidly changing atmospheric conditions,” in *Proc. IEE Proc.-Generation, Transmiss. Distrib.*, Jan. 1995, vol. 142, pp. 59–64.

[44] S. Santoso, *Fundamentals of Electric Power Quality Summer 2010 Edition*, CreateSpace, 2010.

[45] A. Pahwa and C.W. Brice, "Modeling and System Identification of Residential Air Conditioning Load," *IEEE Transactions on Power Apparatus and Systems*, vol.PAS-104, no.6, pp. 1418-1425, June 1985.

[46] S. El-Ferik, S.A. Hussain, F.M. Al-Sunni, "Identification of physically based models of residential air-conditioners for direct load control management," *5th Asian Control Conference*, vol.3, no., pp. 2079- 2087 Vol.3, 20-23 July 2004.

[47] D. Novosel, M.M. Begovic, and V. Madani, “Shedding Light on Blackouts”, *IEEE Power and Energy Magazine*, Vol.2, No.1, 2003, pp. 3-43.

[48] U.S.-Canada Power System Outage Task Force, *Final Report [EB/OL]*, March 31, 2003.

[49] A. Kurita and T. Sakurai, “The Power System Failure on July 23, 1987 in Tokyo”, *Proceedings of the 27th Conference on Decision and Control*, Austin, Texas, 1988.

[50] N. Jantharamin and L. Zhang, "A new dynamic model for lead-acid batteries," *4th IET Conference on Power Electronics, Machines and Drives*, vol., no., pp.86-90, 2-4 April 2008.

[51] H. L. Chan and D. Sutanto. "A new battery model for use with battery energy storage systems and electric vehicles power systems", *IEEE Power Engineering Society Winter Meeting*, volume 1, pp.470-475, (2000).

[52] Z. M. Salameh, M. A. Casacca, and W. A. Lynch. "A mathematical model for lead-acid batteries", *IEEE Transactions on Energy Conversion*, volume 7, no. 1, pp. 93-98, (1992).

[53] M. Dürr, A. Cmden, S. Gair, and J. R. McDonald. "Dynamic model of a lead acid battery for use in a domestic fuel cell system", *Journal of Power Sources*, volume 161, no. 2, pp. 1400-1411, (2006).

[54] G. Celli, S. Mocci, F. Pilo, and M. Loddo, "Optimal integration of energy storage in distribution networks," *2009 IEEE Bucharest PowerTech*, vol., no., pp.1-7, June 28 2009-July 2 2009.

[55] L. Kelly, A. Rowe, P. Wild, "Analyzing the impacts of plug-in electric vehicles on distribution networks in British Columbia," *2009 IEEE Electrical Power & Energy Conference (EPEC)*, vol., no., pp.1-6, 22-23 Oct. 2009.

[56] C. H. Stephan and J. Sullivan, "Environmental and energy implications of plug-in hybrid-electric vehicles," *Environ. Sci. Technol. 42(4)*, pp. 1185-1190, 2008.

[57] J. Song, A. Toliyat, D. Turtle, and A. Kwasinski, "A rapid charging station with an ultracapacitor energy storage system for plug-in electrical vehicles," *2010 International Conference on Electrical Machines and Systems (ICEMS)*, vol., no., pp.2003-2007, 10-13 Oct. 2010.

[58] P. Lombardi, P. Vasquez, and Z.A. Styczynski, "Plug-in electric vehicles as storage devices within an Autonomous power system. Optimization issue," *2009 IEEE Bucharest PowerTech*, vol., no., pp.1-7, June 28 2009-July 2 2009.

[59] R. Angelino, G. Carpinelli, D. Proto, and A. Bracale, "Dispersed generation and storage systems for providing ancillary services in distribution systems," *2010 International Symposium on Power Electronics Electrical Drives Automation and Motion (SPEEDAM)*, vol., no., pp.343-351, 14-16 June 2010.

[60] P.T. Krein, *Elements of Power Electronics*, Oxford University Press, 1998.

[61] N. Mohan, T.M. Undeland, and W.P. Robbins. *Power Electronics: Converters, Applications, and Design Second Edition*, John Wiley, 1995.

[62] H. Sira-Ramírez and R. Silva-Ortigoza. *Control Design Techniques in Power Electronics Devices*, Springer, 2006.

[63] KC200GT High Efficiency Multicrystal Photovoltaic Module Datasheet Kyocera. [Online]. Available: http://www.kyocera.com.sg/products/solar/pdf/kc200gt.pdf

[64] N. Srisaen and A. Sangswang, "Effects of PV Grid-Connected System Location on a Distribution System," *2006 IEEE Asia Pacific Conference on Circuits and Systems (APCCAS)*, vol., no., pp.852-855, 4-7 Dec. 2006.

[65] P. Barker, J. Feltes, and D. Smith, "Determining the Impact of Distributed Generation on Power Systems: Part1 – Radial Distribution Systems", Power Technologies, Inc., 2000.

[66] M. Thomson and D.G. Infield, "Impact of widespread photovoltaics generation on distribution systems," *IET Renewable Power Generation*, vol.1, no.1, pp.33-40, March 2007.

[67] BS EN 50160: "Voltage characteristics of electricity supplied by public distribution systems", British Standards Institution, 2000.

[68] Aluminum Conductor Steel Reinforced (ACSR) Cables Datasheet Alcan. [Online]. Available: http://www.cable.alcan.com/NR/rdonlyres/BC388B10-A9C3-45B6-AA90-F5A9BA9D203D/0/ACSRweb.pdf

Vita

Amir Toliyat was born in Morgantown, West Virginia in 1985. He received the Bachelor of Science in electrical engineering from Texas A&M University, College Station, Texas, in December 2008. He began graduate studies at the University of Texas, Austin, TX in 2009.

His current research interests include smart grids and power electronics.

Permanent Address: toliyat@mail.utexas.edu

This thesis was typed by the author.